Optimization of real-time imaging sequences for MR-guided percutaneous needle interventions with implementation of MR-simulations

Master thesis
Technical Medicine
Nov 2020

J.J. Twilt

Optimization of real-time imaging sequences for MR-guided percutaneous needle interventions with implementation of MR-simulations

Master thesis

Technical Medicine
Nov 2020

J.J. Twilt

Department of Technical Medicine
University of Twente, Enschede, the Netherlands

Department of Imaging
Radboud University Nijmegen Medical Centre, Nijmegen, the Netherlands

In collaboration with

Siemens Healthineers
R&D department of MR-therapy, Erlangen, Germany

Siemens Healthineers
The Hague, The Netherlands

Graduation committee

Chairmen	Prof. dr. J.J. Fütterer *Department of Imaging, Radboud University medical center, Nijmegen, The Netherlands*
Medical supervisor	Prof. dr. J.J. Fütterer *Department of Imaging, Radboud University medical center, Nijmegen, The Netherlands*
Technological supervisors	Dr. ir. F.F.J. Simonis *Department of Magnetic Detection & Imaging, University of Twente, Enschede, The Netherlands* Dr. C.G. Overduin *Department of Imaging, Radboud University medical center, Nijmegen, The Netherlands*
Process supervisor	Drs. N.S. Cramer Bornemann *Department of Technical Medicine, University of Twente, Enschede, The Netherlands*
Supervisor industry	Dr. W. Nijhof *Siemens Healthineers, The Hague, The Netherlands*
External member	L. Molenaar, MSc *Department of Magnetic Detection & Imaging, University of Twente, Enschede, The Netherlands*

Abstract

Objective:
With the introduction of minimally invasive MR-guided interventions, the need for optimal real-time MR-sequences is required to aid in successful needle guidance. Although multiple real-time sequences have been described, consensus on optimal sequence and corresponding sequence settings is lacking. With applications for MR-simulations, this thesis sought out to optimize real-time imaging sequences for MR-guided percutaneous needle interventions with implementation of MR-simulations.

Methods:
In the first objective of this thesis, contrast optimization was performed by simulating the spoiled gradient echo (GRE) with parameter changes for flip angle's (FA) 5°, 10°, 15°, 20° and 25°, and echo time's (TE) of 3, 3.5, 4, 4.5 and 5 ms, balanced steady state free precession (bSSFP) with FA's of 20°, 35°, 40°, 45°, 50° and 55° and half-Fourier acquisition single-shot turbo spin-echo (HASTE) with FA's of 100°, 110°, 120°, 140° and 150°, repetition time's (TR) of 600, 800, 1000, 1200 and 1400 ms and TE's of 71, 79, 91, 99, 127 and 150 ms. Simulations were performed on a human patient model with added lesions at the level of the liver. Lesion to liver contrast, and tissue to tissue contrast was assessed by implementation of the effective contrast to noise ratio (CNR_{eff}). As subobjective the minimal CNR_{eff} for lesion distinction was determined.

In the second objective of the study, simulations were compared with the contrast of an MR-experiment on an abdominal phantom with additional coaxial needle and cryoablation needle. MR-acquisitions of the spoiled GRE, bSSFP and HASTE sequence were simulated on a 3D-model of the abdominal phantom with added needle. Findings from the MR-experiment and simulations were compared on visual differences in contrast, differences in signal tissue ratios relative to liver signal and needle artefact width.

Results:
A minimal CNR_{eff} of 10 for lesion distinction was found. Simulations of the bSSFP and HASTE showed favorable lesion and tissue contrast compared to the spoiled GRE. Highest contrasts were observed at FA variations of 30°-35° for bSSFP. For HASTE, variations in MR-parameters did not show significant change in contrast. Therefore, the HASTE simulation with lowest TR (600 ms) and FA (100°) is argued to be the optimal setting.

Simulations of the spoiled GRE, bSSFP and HASTE show low correspondence based on visual comparison and comparison on tissue signal ratio relative to liver. Similarly, needle artefact width for both coaxial and cryoablation needle were underestimated for spoiled GRE and bSSFP. Similarity in needle artefact width was measured between MR-experiment and simulations of HASTE.

Conclusion:
While lack of agreement between MR-simulations and MR-experiment was observed, the results within this work provide guidance in future optimization for the implementation of MR-simulations within MR-guided percutaneous interventions. For clinical implementation, the observed results should be validated within a MR-environment. Further work to improve the agreement between MR-simulations and the MR-environment encompass optimization of model inputs and optimization of external factors, influencing B0-homogeniety, within the Bloch-simulator.

Contents

Ch. 1

Introduction

1.1 Clinical Background

Minimally invasive procedures have become the desirable method for many surgical interventions to replace invasive surgical treatment. These trends can be observed for multiple cancer types such as prostate, in which an increase in low-grade malignancy does not favor prostatectomy, and kidney and liver, where an increase in non-surgical candidates excludes resection. [1]–[3]

In the last decennia, interventional oncology (IO) has quickly established itself as a promising new field in cancer management, aiding in the introduction of minimally invasive procedures. [4], [5] The field encompasses targeted procedures under image guidance such as biopsies, aspiration, targeted drug delivery and thermal ablation. [6] Within IO, percutaneous guided needle interventions are among the most performed. These procedures describe the application and navigation of a needle under image guidance such as ultrasound (US) and computed tomography (CT) to reach the location of interest.

Recently, more types of percutaneous interventions are performed using magnetic resonance imaging (MRI) guidance. Although MRI is limited by the need for MRI compatible equipment and the limited range of motion inside the bore, MRI is favourable over former techniques such as CT and US due to lack of ionizing radiation, multi-planar imaging capabilities, superior tissue contrast, and the unique ability to directly monitor treatment-induced tissue changes.

Within MRI-guided percutaneous procedures, biopsies are most common. Within the field of prostate malignancies, significant progress has been made in diagnosis. For selected patients, standard transrectal ultrasound-guided (TRUS) multi core biopsies have been replaced with MRI-guided biopsies for accurate navigation towards smaller lesions, reducing the detection rate of clinically insignificant cancers compared to TRUS [1]. Also, for abdominal oncology, MRI-guided biopsies have shown to be an accurate tool for difficult accessible lesions in liver, spleen and kidney. [7], [8]

A second field within the MRI-guided percutaneous procedures is that of ablation therapy. Due to superior tissue contrast and the capability to monitor real-time physiological changes in tissue, MRI ablation therapy has already shown feasible implementation for treatment of prostate cancer, treatment of renal cell carcinoma and liver metastases. [9]–[11]

1.2 State of the art

The success and feasibility of MRI-guided percutaneous procedures is dependent on various factors and differs from those of diagnostic MRI. While diagnostic MRI uses long scanning protocols for visualization of pathology, interventional MRI requires faster image acquisition, reconstruction, and processing to enable real-time guidance during the intervention. Moreover, interventional MRI requires both the visualization of the anatomy as the interventional device to facilitate accurate needle guidance towards the target. [12]

Accurate navigation towards the lesion is dependent on the combined visualization of the anatomy, and the needle. A drawback of MRI-guided needle procedures is the inability to directly monitor the needle position in the MR-image due to its induced perturbation of the main magnetic field. Active tracking methods are described, in which additional hardware can be implemented to track the needle, however, these methods are limited by addition of size, high implementation costs and RF-safety concerns due to heating. [13] For this reason, tracking of the passive needle signal is mostly used in clinical routine.

In clinical practice two main approaches are implemented for MR-guided percutaneous needle interventions. The conventional technique utilizes stepwise advancement of the needle outside the

scanner. After each needle advancement, the patient is moved inside the bore and the location of the needle is verified. This process is repeated until the needle reaches its planned target. The second technique is that of real-time imaging. This technique utilizes near real-time scanning protocols to acquire multiple images per second. The needle can therefore be advanced while the patient remains inside the bore, reducing procedure time.

A real-time technique that is currently widely implemented is described by Rothgang et al. This work describes a rapid technique for freehand MR-guided percutaneous needle interventions (figure 1.1). [6] The technique requires manual selection of the needle entry point and its target point, which are used to automatically align two imaging planes along the needle trajectory and one orthogonal plane at the selected target location. During the intervention, needle tracking can be passively performed by tracking the signal void in the three acquired slices. If the needle deviates from the planned trajectory, manual re-alignment by the technician operating the scanner, needs to be performed. [11]

Figure 1.1 - Example of the workflow described by Rothgang et al. during an MR-guided percutaneous needle intervention. The patient is in the MR scanner with needles in place. At the right side the user interface for the needle guidance is displayed with multiplanar imaging. [6]

For feasible real-time imaging, framerates up to 1 Hz are necessary, based on expert opinion within RadboudUMC. To facilitate real-time needle guidance, rapid gradient echo (GRE) sequences such as steady state free precession imaging (bSSFP) are commonly used. [14] Combined with parallel imaging, framerates of 10 Hz can be achieved while a high signal to noise ratio (SNR) is maintained. [12] The bSSFP sequence is, however, often hampered by banding artefacts due to its susceptibility to magnetic field inhomogeneities occurring at the needle. Another option for fast acquisition is the spoiled GRE. The sequence can create a variety of image contrast by alteration of the echo time, repetition time and flip angle. The sequence is however limited due to the lower SNR compared to the bSSFP sequence. [14]

A disadvantage of the GRE sequences is their association with prominent susceptibility artifacts. Spin-echo (SE) or turbo spin-echo (TSE) sequences, are less prone to these artifacts. [14] When combined with MR-techniques such as parallel imaging and partly-Fourier sampling, relative fast acquisition times can still be achieved. The half-Fourier acquisition single-shot turbo spin-echo (HASTE) is an example of a TSE which creates T2-weighted images with favorable tissue to tissue contrast and less prominent needle artefacts.

While the implementation of MRI-guided percutaneous needle interventions increases, there is no consensus om the optimal sequence to use. [14] It is for this reason that optimization of mentioned sequences is favorable to further improve MRI-guided percutaneous needle interventions and aid in its clinical implementation.

Ch. 2

Research Goals

At RadboudUMC, MRI-guidance during percutaneous needle interventions is used for multiple interventions. As stated, the spoiled GRE, balanced steady state free precession (bSSFP) and half-Fourier acquisition single-shot turbo spin-echo (HASTE) are among sequences that are implemented during these interventions. Similarly, to current literature, consensus on the optimal sequence for this task is lacking. It is therefore proposed to optimize and compare these sequences to improve the implementation of MRI-guided percutaneous needle interventions.

MR-simulations have been an essential part in understanding, developing and prototyping of MRI techniques and sequences in a controlled environment. [15] Up until now, MR-simulations have been used for various purposes such as optimizing sequences [16], training of MR-personnel [17], simulation of 3D-brain volumes [18], simulation of needle artefacts [19] and training of AI-algorithms for segmentation and needle tracking [20]. Within these works, MR-simulations showed to be an advantageous tool to acquire MR-images without access to an MRI-scanner.

To our knowledge, no direct implementation of MR-simulations to optimize sequences for MR-guided percutaneous needle interventions has been performed. Its implementation could, however, provide several advantages, such as elimination of the need of MRI-scanner access and the possibility to implement patient specific models in order to optimize sequence protocols. In addition, as result of the Covid-19 regulations, access to the MRI scanner is limited. For this reason, direct on-site experimentation with MR-sequencing to administer sequence optimization is hampered.

For these reasons, MR-simulations are introduced in collaboration with the MR-therapy research group from Siemens Healthineers (Erlangen, Germany), to perform: *Optimization of real-time imaging sequences for MR-guided percutaneous needle interventions with implementation of MR-simulations*.

To address this goal, two different objectives are formulated.

During the first objective: *Tissue contrast optimization of spoiled GRE, bSSFP and HASTE with the use of MR-simulations*, simulations of the spoiled GRE, bSSFP and HASTE sequence will be performed with different parameter variations to optimize the contrast within the sequences. The aim of this objective is to provide recommendations of sequence settings for optimal distinction between the lesion and its background and various tissues. A subobjective will be to validate the *Rose Model Criterion*, which describes the minimal effective contrast to noise ratio (CNR_{eff}) needed for lesion distinction. To do this, a user experiment is set up, in which visual distinction is associated with its corresponding effective contrast to noise ratio. (chapter 4)

The second objective: *Validation of tissue contrast between MR-phantom experiments and MR-simulations*, is introduced to validate tissue contrast of MR-simulations with measurements from the spoiled GRE, bSSFP and HASTE sequences from MR-phantom experiments. Based on this comparison, the feasibility of accurate MR-simulations is assessed. As a subobjective, both a coaxial needle and a cryoablation needle will be introduced to the model to compare the simulated needle artefact between various sequences and those measured during the experiment. (chapter 5)

The following chapter contains a description of the MRI technique and serves as the technical background before both objectives are answered (chapter 3). The final chapter of this thesis will evaluate the combined outcome of both objectives and will discuss the relevance of this thesis and elaborate on the future perspectives. (chapter 6)

Ch. 3

Technical Background: Magnetic Resonance Imaging

In the following chapter, a selection of topics concerning magnetic resonance imaging (MRI) are explained in more detail to provide the background theory for the following chapters in this paper.

3.1 MRI fundamentals

Magnetic resonance Imaging is a technique that utilizes the nuclear magnetic resonance (NMR) phenomenon to record signals emitted by magnetization decay from the hydrogen nuclei, which is the most abundant nucleus in the human body. The interaction of a sample of nuclei in a magnetic field is described by the net magnetization ($\boldsymbol{M}$). Without $\boldsymbol{B_0}$ the magnetic moments of the nuclei in the sample are randomly orientated. When $\boldsymbol{B_0}$ is applied to the sample, a net alignment of spins to $\boldsymbol{B_0}$ will occur and will result in appearance of $\boldsymbol{M}$ (figure 3.1).

The equilibrium state of the net magnetization is along the $\boldsymbol{B_0}$-field (z-axis) and rotates around its axis with the Larmor frequency $\boldsymbol{f_0}$, which is determined by the strength of $\boldsymbol{B_0}$ and the gyromagnetic ratio of the nuclei (γ). The equilibrium state of $\boldsymbol{M}$ can be affected by applying a radiofrequency (RF) pulse, with a frequency equal to the Larmor frequency of the sample.

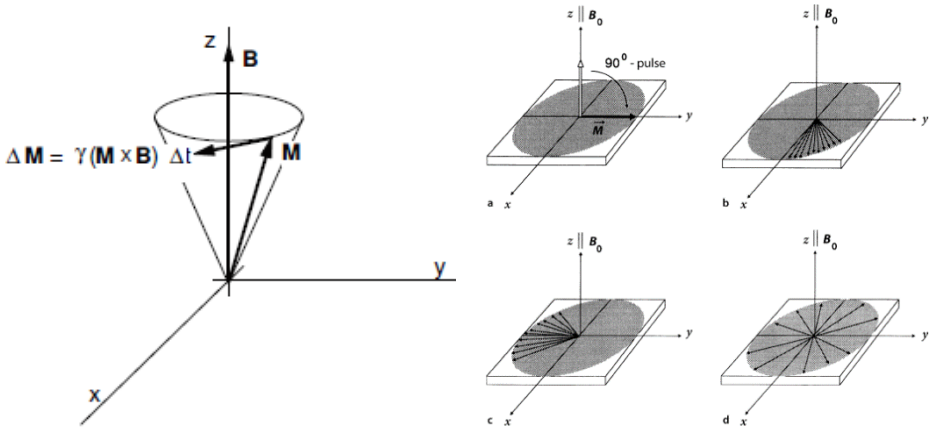

Figure 3.1 - (left) Net magnetization at equilibrium (right) Dephasing of M_{xy} due to T2-relaxation. The various nuclei that compose M align parallel after a 90º RF pulse. Afterwards, due to slight differences in the Larmor frequency, the magnetic components start to dephase. [21]

After excitation, $\boldsymbol{M}$ returns to its equilibrium state due to a process called relaxation. Two different relaxation processes can be distinguished: $\boldsymbol{T_1}$- or spin-lattice relaxation, which describes the regrowth of $\boldsymbol{M_z}$ after excitation, and secondly, $\boldsymbol{T_2}$- or spin-spin relaxation, which describes the decay of the transversal magnetization components $\boldsymbol{M_{xy}}$ (figure 3.1).

Both $\boldsymbol{T_1}$- and $\boldsymbol{T_2}$-relaxation are dependent on the intrinsic characteristics of the nuclei in their surroundings. The influence of both the relaxation processes on the three vector components of $\boldsymbol{M}$ ($\boldsymbol{M_x, M_y, M_z}$) are described by the Bloch equations (eq. 3.1-3.3). The equations show that $\boldsymbol{M}$ exhibits a spiraling precession around $\boldsymbol{B_0}$ with $\boldsymbol{f_0}$ with transversal decay to zero and longitudinal growth to the original magnetization strength ($\boldsymbol{M_0}$). [21], [22]

$$M_x(t) = M_0 e^{-t/T_2} \sin f_0 t \quad (3.1)$$

$$M_y(t) = M_0 e^{-t/T_2} \cos f_0 t \quad (3.2)$$

$$M_z(t) = M_0(1 - e^{-t/T_1}) \quad (3.3)$$

Because MR experiments are conducted on macroscopic samples, transversal relaxation is not only dependent on the $\boldsymbol{T_2}$ tissue characteristics, but also on fluctuations and inhomogeneities in the local magnetic field (ΔB_{inhom}). This causes the effective relaxation ($\boldsymbol{T_2}$*) to be shorter than the tissue specific $\boldsymbol{T_2}$-relaxation. The relationship between $\boldsymbol{T_2}$ and $\boldsymbol{T_2}$* can be expressed by (eq. 3.4):

$$\frac{1}{\boldsymbol{T_2}^*} = \frac{1}{\boldsymbol{T_2}} + \gamma \Delta B_{inhom} \quad (3.4)$$

Significant perturbations in $\boldsymbol{B_0}$ (ΔB_{inhom}) are often caused by para-, super- or ferromagnetic materials. Field perturbations are therefore also induced by interventional needles, due to their ferromagnetic material composition. The influence of the needle on $\boldsymbol{B_0}$ can be explained by understanding the field perturbation around the needle. This is visualized in figure 3.2, with a needle orientated perpendicular to $\boldsymbol{B_0}$. As shown, the local magnetic field is increased in the voxels adjacent, and in line, to the needle, inducing a higher precession rate. Contrarily, voxels perpendicular to the needle precess with lower frequencies. [23] The induced differences in frequency cause a shift in k-space for these voxels, causing shifting of image signal and therefore artefact appearance. Besides the orientation and the strength of $\boldsymbol{B_0}$, the size of the artefact is dependent and proportional to the change in susceptibility, $\boldsymbol{TE}$ and the pixel bandwidth (eq 3.5). [24]

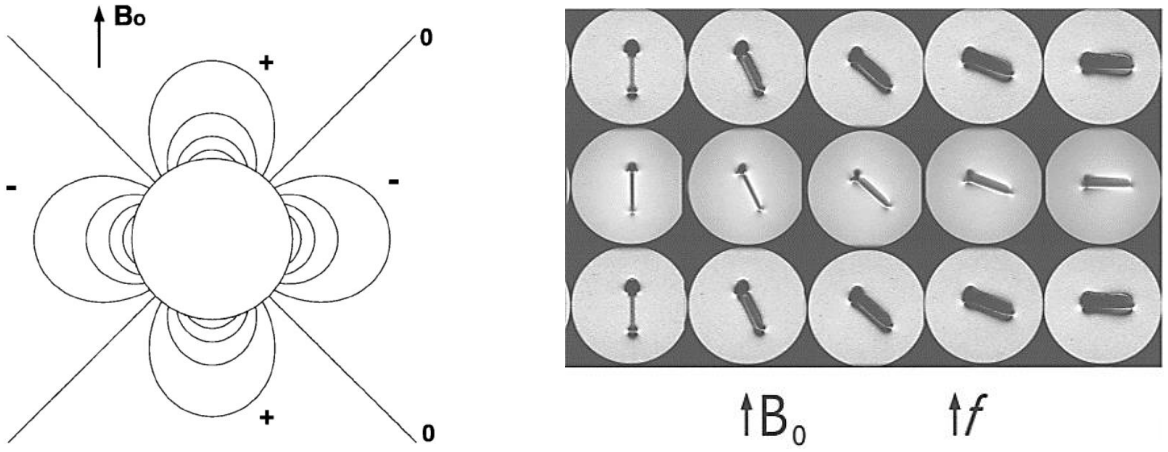

Figure 3.2 - (left) Influence of a metal needle on the magnetic field with its orientation perpendicular to $\mathbf{B_0}$. Spins adjacent and left/right of the needle precess with a lower frequency. Spins adjacent and above/below the needle precess with a higher frequency. [23] (right) Effects of varying angle to $\mathbf{B_0}$ on artefact size for spoiled GRE (upper row), SE (middle row) and GRE (lower row) [24]

$$Susceptibility\ Artefact\ Size \propto \frac{(\Delta\ Susceptibility\ ) \cdot \boldsymbol{B_0} \cdot \boldsymbol{TE}}{Pixel\ Bandwidth} \quad (3.5)\ [24]$$

3.2 MRI sequences

3.2.1 Spin-Echo

As explained, due to local field variations and inhomogeneities, transversal magnetization relaxes not with the tissue specific $\boldsymbol{T_2}$-relaxation but faster with $\boldsymbol{T_2}$*. To determine tissue specific $\boldsymbol{T_2}$ contrast, it is important to compensate for these inhomogeneities. This can be done with the so-called spin-echo (SE) sequence. The SE signal is described by eq. 3.6. The intensity is proportional to $\boldsymbol{PD}$ (proton density), $\boldsymbol{T_1}$, which influence is increased when $\boldsymbol{TR}$ decreases, and $\boldsymbol{T_2}$, which influence is increased when TE increases.

$$S_{SE} = PD \cdot [1 - e^{-T_R/T_1}] \cdot e^{-T_E/T_2} \text{ (3.6) [21]}$$

Acquisition of a true SE-sequence with $\boldsymbol{T_2}$-weighting acquires long acquisition times (AT). To improve AT, a turbo variant (turbo-SE) can be used. In this case, k-space data is obtained after a single RF-excitation combined with long echo trains. The HASTE sequence is a variant of a turbo-SE sequence. The sequence uses the single-shot technique, combined with partial Fourier sampling, in which k-space is not fully sampled and partly estimated by phase symmetry, to achieve fast image acquisition. Due to the longer $\boldsymbol{TE}$'s, HASTE is typically $\boldsymbol{T_2}$-weighted.

3.2.2 Gradient Echo

The gradient echo (GRE) sequence is a method in which only the gradients are used to dephase and refocus $\boldsymbol{M}$ to create an echo of the MR-signal. In contrast to the SE-sequence, the influence of field variations and inhomogeneities are not compensated with GRE-sequences. The gradient reversal only refocuses the spins that have been dephased by the gradient itself. The transversal magnetization is therefore not dependent on $\boldsymbol{T_2}$ but on $\boldsymbol{T_2}$*.

The fast low-angle shot with acronym FLASH, is an example of a spoiled GRE. [25] The sequence utilizes a low flip angle and a spoiling gradient at the end of $\boldsymbol{TR}$, in which transversal magnetization is destroyed. When the sequence is repeated for several cycles, a steady state of the longitudinal magnetization ($\boldsymbol{M_z^{ss}}$) arises. As the transversal magnetization is disrupted after $\boldsymbol{TR}$, the major use of FLASH is to produce $\boldsymbol{T_1}$-weighted images. However, $\boldsymbol{T_2}$*-weighted images can be achieved by appropriate selection of the acquisition parameters $\boldsymbol{TR}$, $\boldsymbol{TE}$ and flip angle (**α**) (eq 3.7).

$$S_{FLASH} = PD \cdot \frac{(1 - e^{-T_R/T_1}) \sin\alpha}{1 - e^{-T_R/T_1} \cos\alpha} \cdot e^{-T_E/T_2*} \text{ (3.7) [21]}$$

Balanced steady state free precession (bSSFP) is a sequence which uses gradient refocusing along all three axes. This creates a balanced signal, in which the net induced gradient is zero. By succession of RF pulses, transversal and longitudinal magnetization components will be mixed, as both magnetization components are greater than zero. This causes signal intensity to be a combination of both $\boldsymbol{T_1}$ and $\boldsymbol{T_2}$.

An interesting aspect of the bSSFP is that the GRE sequence is less susceptible to field inhomogeneities when $\boldsymbol{TE = TR/2}$. This makes image signal to be more dependent on $\boldsymbol{T_2}$ than $\boldsymbol{T_2}$*. [26] The signal equation of bSSFP is shown in eq. 3.8.

$$S_{bSSFP} = PD \cdot \frac{\sin\alpha}{1 + T_1/T_2 + (1 - T_1/T_2)\cos\alpha} \cdot e^{-T_E/T_2} \text{ (3.8) [21]}$$

3.3 MRI simulations

MRI simulations are based on solving the Bloch-equations for a voxel-based model with various position and time dependent tissue characteristics. The Siemens Healthineers implementation of the Bloch-simulator used during this study is based on the works of Stöcker et al. [27] Bloch equations in cylindrical coordinates (M_r, φ, M_z) are solved for individual voxels at position r at time t, with physical properties (eq. 3.9): [27]

$$P(r,t) = \{M_0, T_1(r,t), T_2(r,t), T_2^*(r,t), \Delta\omega(r,t), \chi(r,t)\} \text{ (3.9)}$$

With M_0, equilibrium magnetization, T_1, T_2 and T_2^* the relaxation times, χ magnetic susceptibility, and $\Delta\omega$ a small random off-resonance term. Besides voxel input, the amount of simulated spins per voxel is determined by the user. An increase in spins per voxel generates an increase in signal to noise, however, additionally induces an increase in computational load.

The integration over all transverse components in the coil volume yields the time dependent MR-signal for corresponding receiver coil. Images are then generated from the k-space data.

Ch. 4

Tissue contrast optimization of spoiled GRE, bSSFP and HASTE for MRI-guided needle interventions using MR-simulations

4.1 Introduction

The first objective of this study is to use MR-simulations to optimize tissue contrast for the spoiled GRE, bSSFP and HASTE sequence for MRI-guided percutaneous needle interventions. During this objective, the three sequences will be simulated with various MRI-parameter variations in order to determine which sequence settings provide recommended contrast during interventions.

For simulation purposes, a model needs to be implemented to assess tissue contrast optimization. Recently, MRI-guided liver biopsies have been introduced at RadboudUMC for lesions difficult to reach with other imaging modalities. For the MR-guided biopsies, the optimal MR-sequence still needs to be found. In addition, modelling of the liver is more attainable compared to for instance the prostate, because liver can be modelled by a singular homogenous structure instead of the multiple zones comprising the prostate. It is for these reasons that tissue contrast optimization is assessed for the liver and corresponding anatomy.

For contrast assessment a measure needs to be introduced to determine the distinction between lesion and background tissue, and tissues to surrounding tissues and vessels. As not only the contrast of the lesions compared to its background aids in lesion distinction, but also the size of the lesion itself, the *Rose Model*, which describes the minimal effective contrast to noise ratio (CNR_{eff}) necessary for lesion distinction will be applied and evaluated in a user experiment. [28] Based on this experiment, the minimal CNR_{eff} is determined to sufficiently distinguish lesion from its background and will be implemented as criterion to assess the optimization of the three simulated sequences. For this reason, this subobjective will be performed prior to sequence optimization.

This chapter will be closed with a discussion on the simulation outcomes and a comparison between the three sequences.

4.2 Methods

4.2.1 Materials

Simulation Model

The *AustinMan*, an open-source voxel model constructed from a human dataset, was used as a human patient model for the simulations. [29] In this model each voxel is assigned a specific material ID, which is used for assignment of tissue specific characteristics such as proton density and T1- and T2-relaxation values.

The model was extended with five lesions with diameters of 3, 5, 10, 15 and 20 mm, respectively. The lesions were modelled as 3D spheres in a CAD program (Solid Edge 2020, Academic Edition, Siemens Digital Industries Software) and imported as a mesh in MATLAB (R2018b, The Mathworks Inc). The meshes were then voxelized and positioned at various coordinates inside the selected model slice in voxels containing liver. The lesions were then assigned with their own specific tissue ID number. In the

final human model, one transversal slice through the liver and lesions was selected to be used during simulations.

Tissue Characteristics

As input for the simulations, specific T1- and T2-relaxation times, proton density, magnetic susceptibility and chemical shift values were obtained from literature and assigned to the model. For the simulation of the lesions, the mean T1 and T2-relaxation values of hepatocellular carcinoma and hepatic metastasis observed by the work of Farraher et al. were used. [30] For some values T1- and T2-relaxation times were only available for 1.5T experiments (appendix A). For those values, the T1-relaxation was increased by 25% to extrapolate to a field strength of 3T. [31] A list of all voxel materials used during the simulations can be found in appendix A.

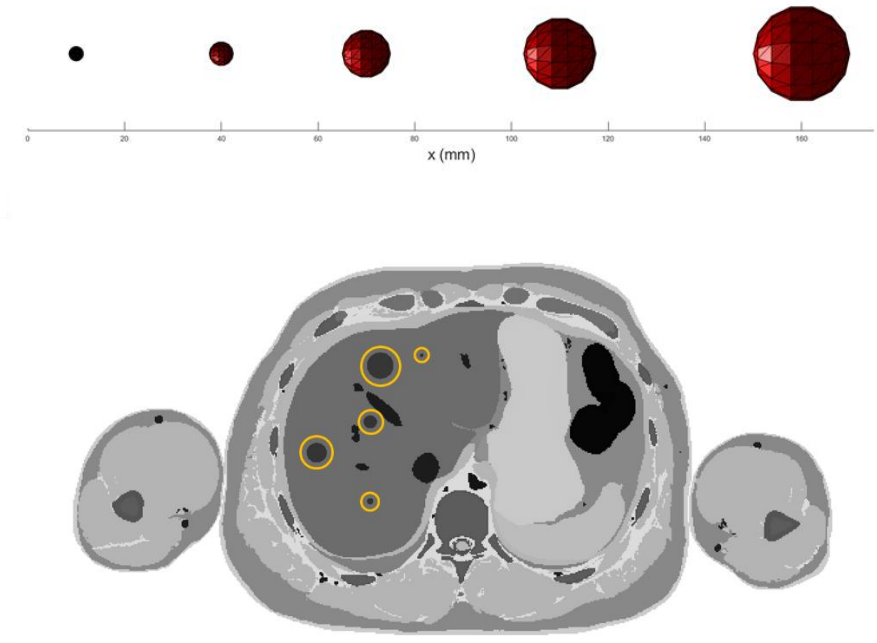

Figure 4.1 – Addition of the 3D-lesions to the human model. (top) Mesh visualization of the lesions (red) with 3 mm, 5 mm, 10 mm, 15 mm and 20 mm diameter, modelled to be placed in the liver. (bottom) Selected transversal slice in the patient model. Different grey values represent different tissue materials. The five lesions are emphasized (yellow annotations).

4.2.2 Rose Criterion Validation – Effective CNR for lesion distinction

The distinction between target and tissues can quantitively be made using the contrast to noise ratio (CNR). CNR is a metric that describes how much the differences of a region of interest (ROI) and corresponding background signal rise above the image noise (eq. 4.1):

$$CNR = \frac{\left|S_{ROI} - S_{background}\right|}{\sigma} \quad (4.1)$$

With, S_{ROI} signal intensity of the ROI, $S_{background}$ signal intensity of the background tissue and σ standard deviation of the image noise. Along with contrast and the image noise, an increase in the ROI size will increase the detectability of the lesion. To account for the influence of lesion size on lesion distinction, *The Rose Model* is introduced. *The Rose Model* introduces the effective CNR (CNR_{eff}), which describes the relationship between the CNR and the area of the region of interest (ROI) (eq. 4.2):

$$CNR_{eff} = \sqrt{N_{ROI}}CNR \ (4.2\ )$$

With N_{ROI} the number of pixels compromising the ROI. In addition, the *Rose Criteria* is introduced which describes the minimal CNR_{eff} needed for lesion detection. Various experiments with observers have shown that a CNR_{eff} between 3-5 suffices for lesion detection. [28]

An experiment was set up to determine and validate the CNR_{eff} for lesion distinction. A simulated MR-image of the human patient containing liver and lesions was selected. On the selected slice, Gaussian noise was increasingly added in fifty steps creating a dataset with fifty images with maximum SNR of 175 and minimum SNR of 1, with SNR defined as the mean lesion signal divided by mean noise measured from the image background.

Four readers, experienced with MR-guided interventions, were then asked to determine the cut-off value for lesion distinction for all five lesions. For this, the four readers were allowed to scroll through the set of deteriorated MR-images and select at which slice number the lesion was still distinguishable from its background (figure 4.2).

Once the experiment was performed the CNR_{eff} was calculated for the lesions in the MR-noise dataset. ROI's were selected for the lesions. In addition, for every lesion a background ROI was selected in the liver near the corresponding ROI. CNR_{eff} was calculated with eq 4.1 and 4.2, with S_{ROI} the mean of the corresponding lesion ROI, $S_{background}$ containing the mean of the background ROI of corresponding lesion and N_{ROI} the number of pixels compromising the lesion ROI. Lastly, CNR_{eff} of the lesions was noted for the slices selected by the users.

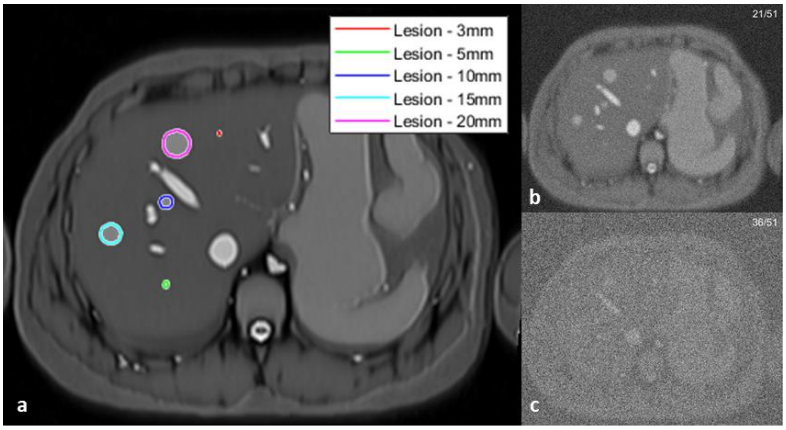

Figure 4.2 - (a) Simulated slice with ROI's of the five lesions. Two examples of slices in de dataset with (b) SNR of 10 and (c) SNR of 5, used during the experiment to determine the visibility threshold.

4.2.3 Sequence optimization strategy

For optimization of the spoiled GRE, bSSFP and HASTE sequences, various strategies were applied. Based on the sequence equation, flip angle has the largest influence on image contrast for both the spoiled GRE and bSSFP sequence (eq. 3.7,3.8). Optimal contrast between liver and lesions was estimated by calculating the flip angle with highest theoretical signal intensity (eq. 3.7,3.8) difference between liver and lesion. For this, TR was minimized with a fixed TE, while signal intensities were determined for various FA's. These figures served as reference for the simulated flip angle variations and are provided in appendix A2.

Further experimentation with the GRE contrast was performed by altering the echo time. Changes in TE will influence the second term in eq. 3.7 and will give the image more T2-star weighting instead of T1. Protocol restrictions imposed by the scanner, however, limited further variations with the bSSFP sequence.

For HASTE different optimization strategies were implemented compared to the spoiled GRE and bSSFP sequences. Since HASTE is restricted by lower framerates (approximately 2 Hz [32]) compared to the GRE sequences, and is additionally restricted by a higher risk on reaching SAR limits due to the repeated RF-pulses, the influence on lower TR's and FA's on image contrast and SAR limits was investigated by implementing parameter variations between 600-1400 ms and 100-154°. Further contrast optimization was performed by changing the effective TE, which increases the contrast of tissues with longer T2-times.

MRI simulations

MRI simulations were performed by an external operator on a Siemens workstation which reads Siemens MR-protocols and implements Bloch-simulations as described by Stöcker et al. [27] Siemens *BEAT Interactive* with GRE and bSSFP (Siemens workname: *TrueFISP*) contrast and HASTE protocols were extracted from a 3-T MR-system (Magnetom Skyra, Siemens, Erlangen, Germany). Protocol changes were made using the *protocol editor* (POET) environment of IDEA and a virtual MR-simulation station.

Simulations were performed with the following settings: For the spoiled GRE, FA variation of 5° to 25° and TE variations of 3 to 5 ms were performed. During the TE variations, TR was increased from 309 to 431 ms as well due to scanner limitations. As a result, acquisition times were lengthened, and overall T2-star weighting increased. bSSFP variations were performed for FA 20° to 55°. For HASTE, FA variations of 100° to 154°, TR variations of 600 to 1400 ms and TE variations of 71 to 150 ms were performed.

4.2.4 Analysis

Quantification metrics

Lesion to liver and tissue to tissue contrast was measured by CNR_{eff}. Lesion masks were automatically determined by thresholding the selected slice of the patient model on the lesion tissue ID's. Corresponding masks were then scaled to fit the field of view of the simulated slices. For other tissues, thresholding the patient model for corresponding tissue ID's would create insufficient results. Therefore, manual ROI's were selected for air (background noise), liver, bone, muscle, fat, and vasculature.

CNR_{eff} of the lesions was determined by solving eq. (4.1) with S_{ROI} the mean signal intensity of the lesion, $S_{background}$ the mean signal intensity of liver and σ the standard deviation of air. Thereafter, eq. (4.2) was solved with N_{ROI} the number of pixels of the lesion ROI. For tissue contrast the CNR_{eff} was determined by solving eq. (4.1) with S_{ROI} the mean signal intensity of the tissue, $S_{background}$ and σ set to liver and air, followed by solving eq. (4.2) with N_{ROI} the number of pixels of the tissue ROI.

In addition, the signal to noise (SNR) was used to assess image quality. Since the noise of the simulations is dependent on the amount of spins per voxel simulated (section 3.3), SNR could only be compared within similar sequence protocols in which the spins per voxel was set to the same number. Therefore, a ratio (SNR_{ratio}) was implemented which compared the SNR found in corresponding simulation to the simulation of the baseline protocols of the spoiled GRE (TE=2.4ms, TR=275ms, Echo Spacing (ES)=4.5ms, FA=12°), bSSFP (TE=1.5ms, TR=188ms, ES=2.9ms, FA=30°) and HASTE (TE=51ms, TR=600ms, ES=4ms, FA=154°). The SNR_{ratio} was determined for all lesion and tissue ROI's by firstly calculating the SNR of selected ROI, followed by division of the SNR of selected ROI in the baseline simulation. The mean SNR_{ratio} was then determined to provide overall image quality assessment.

4.3 Results

The first objective is to optimize the spoiled GRE, bSSFP and HASTE sequence with the use of MR-simulations. To assess the simulations, the minimal CNR_{eff} for lesion distinction will be applied. Hence, the results of the validation of the minimal CNR_{eff} needed for lesion distinction is firstly reported.

4.3.1 Rose Criterion validation

The *Rose Criterion* was introduced to determine the minimal CNR_{eff} for sufficient discrimination between lesion and background tissue. During the experiment, an average minimal CNR_{eff} in which lesion to liver contrast is sufficient for distinction for most users, was sought. The results of this experiment are shown in table 4.1. and provide the minimal CNR_{eff} value in which lesion to liver contrast is sufficient for distinction by the individual users.

Inspection of the table shows that the CNR_{eff} is higher than the *Rose Criterion* for all five lesions with the lowest mean CNR_{eff} found for the 3 mm lesion (6.3) and the largest found for the 15 mm lesion (10.3). The mean CNR_{eff} found for all lesions and all users was 10.0. This value was also used as the minimal CNR_{eff}, defined as the minimal value for distinction between lesion to liver for most users.

Table 4.1 - Minimal CNR_{eff} for lesion to liver distinction determined during the threshold experiment by the four readers for five lesions with given mean and standard deviation. A small variation was observed within the CNR_{eff} for lesions of 3 and 5 mm. Two clear outliers can be observed, in which the CNR_{eff} threshold determined by reader C for lesion of 15 and 20 mm diameter, is approximately twice as large as the determined CNR_{eff} by the other readers.

Reader	Les. 3 mm	Les. 5 mm	Les. 10 mm	Les. 15 mm	Les. 20 mm	*Mean*
A	5.4	6.9	6.6	11.7	10.2	
B	8.6	6.9	8.8	11.7	10.2	
C	4.6	9.8	11.8	23.9	23.5	
D	6.6	6.9	8.4	10.3	7.6	
Mean	6.3	7.6	8.9	14.4	12.9	**10.0**
Std	1.7	1.4	2.2	6.3	7.2	

4.3.2 Sequence optimization

In total, twenty-eight simulations were performed for experimentation with the sequence settings for sequence optimization. Table 4.2 provides an overview of the base protocols and the different parameter variations performed during the simulations of the three sequences. Acquisition times (AT) were largely kept under 1 Hz, which is a feasible minimal framerate for real-time imaging (section 1.2). AT can be increased by incorporating parallel imaging techniques such as GRAPPA, which could increase AT with approximately a factor of 2-3. Since GRAPPA reconstruction could not be simulated, parallel imaging was turned off. According to the MRI-simulation station, SAR limits were not reached for the protocols.

Table 4.2 – Simulated sequence protocols for optimization purposes with given parameters settings for echo time (TE), repetition time (TE), echo spacing (ES), flip angle (FA), field-of-view (FOV), acquisition (Acq) matrix, partial fourier sampling and acquisition time (AT).

Sequence	TE/TR (ms)	ES (ms)	FA (°)	FOV (mm)	Acq Matrix	Partial Fourier	AT (s)
GRE *Baseline*	2.4 / 601	4.5	12	300x300	161x160	6/8	0.7
GRE *FA variations*	2.4 / 601	4.5	5, 10, 15, 20, 25	300x300	161x160	6/8	0.7
GRE *TE variations*	3 / 675, 3.5 / 742, 4 / 808,	5.0 5.5 6.0	15	300x300	161x160	6/8	0.7 0.8 0.9

	4.5 / 875, 5 / 941	6.5 7.0					0.9 1.0
bSSFP *Baseline*	1.5 / 380	2.9	30	300x300	161x160	6/8	0.4
bSSFP *FA variations*	1.5 / 380	2.9	20, 35, 40, 45, 50, 55	300x300	161x160	6/8	0.4
HASTE *Baseline*	51/600	4.0	154	308x251	192x125	6/8	0.6
HASTE *FA variations*	51 / 600	4.0	100, 110, 120, 140, 150	308x251	192x125	6/8	0.6
HASTE *TR variations*	51 / 800, 51 / 1000, 51 / 1200, 51 / 1400	4.0	150	308x251	192x125	6/8	0.8 1.0 1.2 1.4
HASTE *TE variations*	71 / 600, 79 / 600, 91 / 600, 99 / 600, 127 / 600, 150 / 600	4.0	154	308x251	192x125	6/8	0.6 0.6 0.6 0.6 0.6 0.6

Spoiled GRE optimization

Variations in Flip Angle

Simulations implementing flip angle variations with flip angles 5°, 10°, 12° (baseline protocol), 15°, 20° and 25° were performed for spoiled GRE optimization. Figure 4.4 (pg. 17) shows examples of simulations ran with FA's of 5°, 15°, and 25°. For all FA's, lesions were visually not distinguishable from liver tissue and did not exceed the minimal CNR_{eff} of 10, making the spoiled GRE less feasible for MR-guided interventions. With increased FA, discrimination between tissues increased. Highest CNR_{eff} for tissues were found at FA=15° (minimal CNR_{eff} of 32 for bone, maximal CNR_{eff} of 272 for fat), providing optimal image contrast when lesion distinction is discarded.

The SNR_{ratio} was determined for all lesions and tissues. All lesions and tissues showed similar progression, that is, when FA's increase, the SNR_{ratio} decreases. The mean SNR_{ratio} is highest at FA=5° (mean SNR_{ratio}=1.6) and decreases to a mean SNR_{ratio} of 0.7 at FA=25°.

Variation in Echo Time

For the TE parameter variations, increase in TE also induces an increase in the echo spacing (ES) and TR (table 4.2), therefore limiting sole manipulation of TE. Increase in TE increased the distinction of the lesion with 15- and 20-mm diameter minimally (figure 4.5 on pg. 17). From TE of 4 ms and higher, the CNR_{eff} of these lesions surpassed the threshold value (CNR_{eff}>10. For the tissues, CNR_{eff} did not increase significantly over the range of varied TEs (3 to 5 ms).

Interestingly the SNR_{ratio} increases together with an increase in TE. This can be explained by a correlated increase in TR (309 to 431 ms). At the lowest TE of 3 ms the mean SNR_{ratio} is comparable to the SNR of the baseline protocol. At TE=5 ms the mean SNR_{ratio} was increased to 1.5. Visual inspection does not however indicate strong differences between SNR within the different TE simulations.

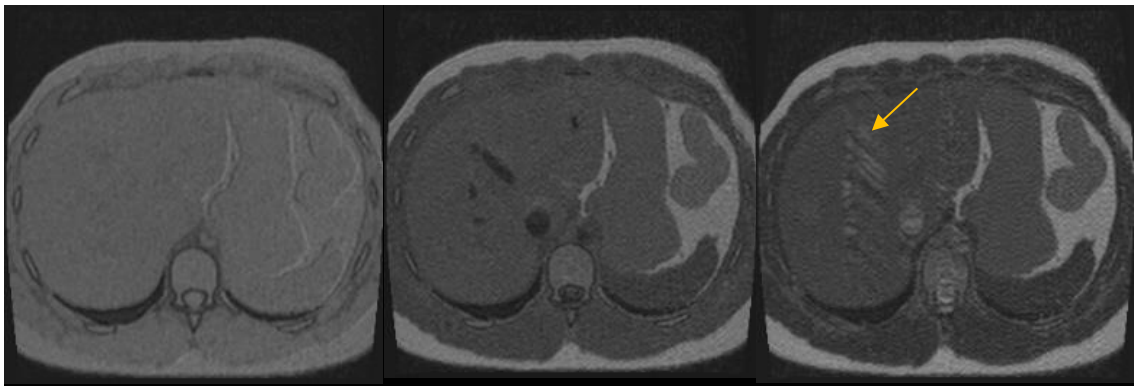

Figure 4.4 - GRE simulations with FA parameter variations of FA's 5°, 15°, and 25° (left to right). A lack of lesion to liver distinction is observed. At FA=25°, artefacts appeared through the ROI measurements (near the arrow), wrongfully leading to effective CNR of lesions 10, 15, exceeding the minimal CNR_{eff} threshold. Within the range of FA's, mean SNR_{ratio} decreases from 1.6 (FA=5) to 0.7 (FA=25).

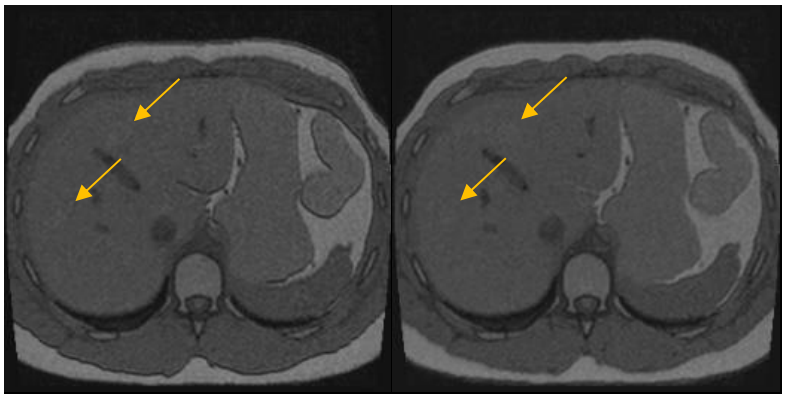

Figure 4.5 - GRE simulations with TE parameter variations of TE's 4 and 5 ms (left to right). No strong differences in contrast are apparent, however, minimal distinction of the lesions (CNR_{eff}>10) is observed (arrows).

Overall, the GRE sequence could not create a strong distinction between liver and lesion, limiting its potential for MRI-guided interventions. The results showed that an increase in FA show minimal change in lesion to tissue distinction but does increase tissue to tissue contrast. Furthermore, increasing the TE does seem to provide minimal increase in liver to lesion contrast.

bSSFP optimization

Variations in Flip Angle

Simulations were performed with FA's of 20°, 30° (baseline protocol), 35°, 40°, 45°, 50° and 55°. Figure 4.7 illustrates six examples of the simulated bSSFP images. Lesions are visible among all flip angle variations (CNReff >10), which increases the applicability for MR-guided interventions. The highest contrast was found at FA=35 for bone, and muscle, with respectively CNR_{eff} of 652 and 260.

The mean SNR_{ratio} between FA's and the baseline protocol decreases at higher FA's. The mean SNR_{ratio} at FA=20° was 1.6 and decreased to 0.4 at FA=55°. Striking are the image artefacts in the phase encoding direction especially distinguishable at higher FA's (arrows in figure 4.7).

Overall, bSSFP shows favourable lesion distinction with optimal contrast for liver and muscle at FA=35°. Higher FA's are not recommended due to significant loss in SNR and liver to muscle contrast.

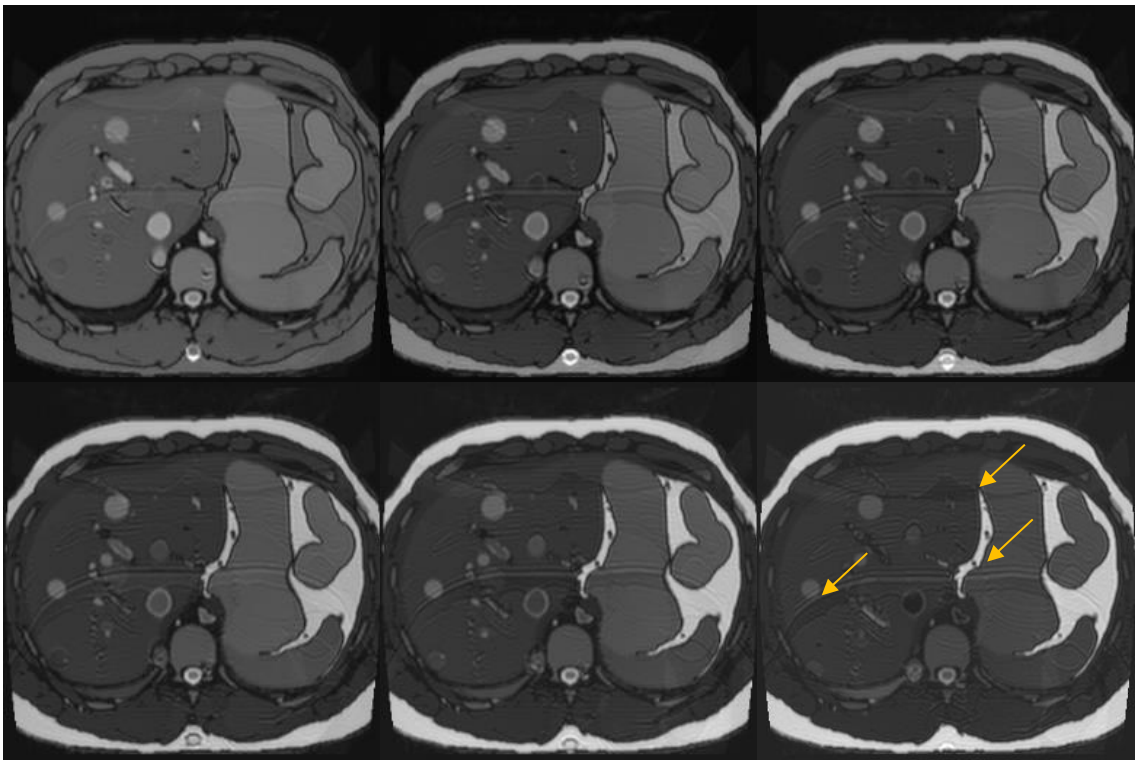

Figure 4.7 - bSSFP simulations with parameter variations of FA's (row 1: left to right) 20, 30, 35, (row 2: left to right) 40, 45 and 55°. Significant decrease in SNR is visible with higher FA's. Throughout the simulations, artefacts in phase encoding direction appear. These are annotated (arrows) at FA=55°.

HASTE optimization

For the HASTE sequence optimization was performed to determine the influence of lower FA's on image signal and lower TR's to make the sequence more feasible for real-time image acquisition. Change in contrast was further investigated by implementation of variations in effective TE.

Variations in Flip Angle

Simulations with FA changes were performed for FA's 100°, 110°, 120°, 140°, 150° and 154° (baseline). Visible assessment of the simulations indicates clear distinction between lesions and liver (figure 4.8) and surpassed the minimal CNR_{eff} for lesion distinction. Tissue to tissue contrast was overall low, with liver to muscle CNR_{eff} of 9 at FA=150°, signifying the lack of clear distinction. No clear differences with the baseline protocol were seen in the SNR_{ratio} of the lesions and tissues (SNR_{ratio} between 0.8 and 1.1).

Variations in Repetition Time

For assessment of lowering TR on tissue and lesion visibility, TR variations with TR's of 600, 800 1000, 1200 and 1400 ms were performed. Results showed that there was no change in CNR_{eff} and SNR_{ratio} for the different TR times, indicating that lower TR's could be used to further speed up acquisition time for HASTE during MR-guided interventions (600ms compared to 1400ms).

Variation in Effective Echo Time

Simulations with different effective TE's of 71, 79, 91, 99, 127 and 150 ms were performed. Visual inspection shows an increase in contrast of tissues with longer T2-relaxation times such as lesion, fat, and blood (figure 4.9). As expected, SNR would decrease when TE would increase. At TE=71 ms, mean SNR_{ratio} decreased to 0.5. Although lesion contrast improves, the strong decay in SNR_{ratio} causes longer TE's to compromise overall image quality. Extending TE is therefore less feasible for MR-guided interventions.

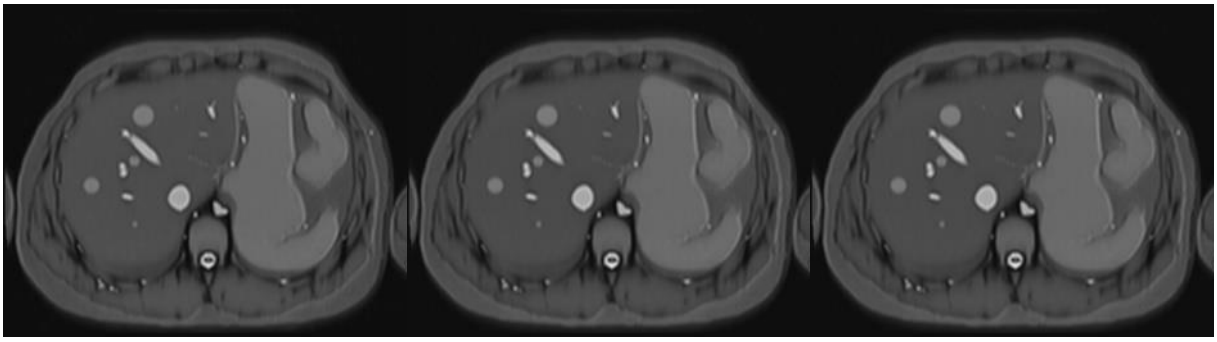

Figure 4.8 - HASTE simulations with parameter variations of FA's (left to right) 100°, 120°, 150°. Clear distinction of the lesions is observed, while tissue to tissue contrast is low. No significant changes in SNR are seen between the various FA's.

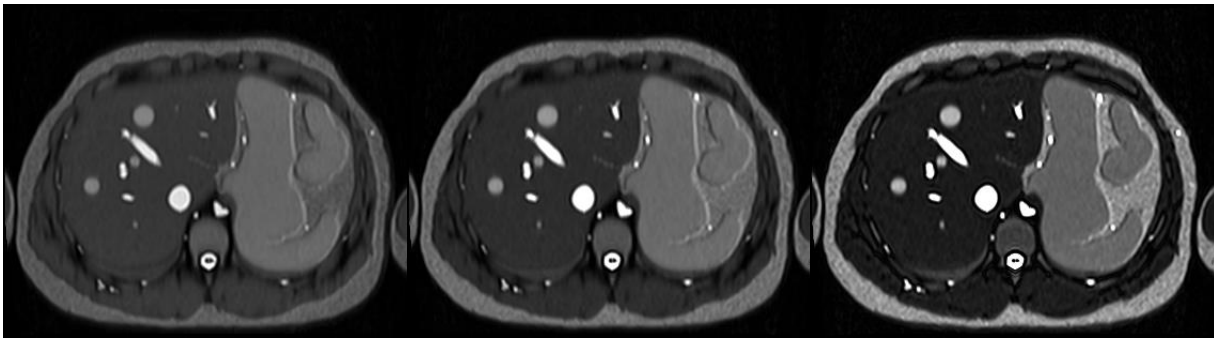

Figure 4.9 - HASTE simulations with parameter variations of the effective TE (left to right) 71, 99 and 150 ms. Increase of the effective TE shows increased contrast in tissues with longer T2-relaxation times, while the SNR is significantly lower compared to the baseline protocol. (at 71ms, SNR_{ratio}=0.5, at 150 ms, SNR_{ratio}=0.4)

4.4 Discussion

The first goal in this thesis was to optimize the lesion and tissue contrast of the spoiled GRE, bSSFP and HASTE sequence with MR-simulations, to provide recommendations for MRI-guided percutaneous needle interventions. Results showed that lesion distinction was insufficient for the spoiled GRE simulations in which changes in FA and TE showed minimal difference in distinction, making this sequence less feasible for MR-guided interventions. For both the bSSFP and HASTE sequence, clear distinction between the lesion and liver, and tissue to tissue was observed. bSSFP showed optimal contrast for lesion and tissues at FA's between 30° and 35°. For the HASTE sequence, FA changes and TR changes showed minimal changes whereas signal to noise ratio would greatly decrease at higher TE's. For this reason, optimal settings for the HASTE could be argued to be at the lowest simulated FA (100°) and TR (600 ms), without exceeding the SAR limits.

The high distinction for lesion to liver found for the bSSFP and HASTE sequence, corresponds with previous work. Stattaus et al. investigated feasibility of MR-guided abdominal biopsies at 1.5-T. HASTE outperformed bSSFP and turbo-FLASH with inversion recovery on lesion to liver distinction. [32] Work of Remp et al. compared lesion to liver distinction between spoiled GRE and bSSFP for real-time MR-guided radiofrequency applicator placement. Although the work presented showed favourable distinction for hepatocellular carcinoma (HCC) with bSSFP, T1-weighted spoiled GRE showed as the better sequence to distinct liver metastases. [33] This does not correspond with our findings, in which low distinction for the spoiled GRE was observed.

Different findings for the spoiled GRE compared to earlier work can be attributed to the simulation model and corresponding T1, T2 and proton density (PD) inputs. In our work, liver lesions were modelled by implementation of the observed T1- and T2-times by Farraher and colleagues. [30] In their work, both

HCC's and metastases were grouped and showed a mean of 609 ± 133 ms, indicating a great variety in measured T1-times. By extrapolation to a 3-T field, the implemented T1-time for lesion only differed 50 ms from the T1-time of liver (760 ms vs 810 ms). Combined with a similar proton density assignment in the model, low to no distinction between the lesion and liver in the spoiled GRE was observed.

For optimal sequence settings, the framerate did not exceed 1 Hz. With introduction of parallel imaging techniques such as GRAPPA, acquisition times can be lowered with factor 2 or 3 [12]. This is promising, as framerate could be kept around 1 Hz while implementing the often-used clinical method for real-time needle guidance, acquiring three imaging planes along the needle trajectory. [6] GRAPPA has additional advantages for HASTE in which the shortening of the readout train also reduces blurring. Due to the decreased amount in k-space sampling, GRAPPA can, however, also introduce decrease in SNR. [34] This can specifically also disadvantage HASTE, in which the combination with low FA, image SNR may be too low for feasible imaging. Due to the advantages of GRAPPA, its implementation is suggested during interventions, with for HASTE the condition that SNR is still feasible for lesion and tissue distinction.

To further investigate optimal sequence settings, verification whether the SAR limits will be exceeded with applied protocols needs to be performed outside the simulation environment. Especially for the HASTE sequence, the found results are greatly dependent on SAR. User experience at the Radboud indicates that these limits will be exceeded when FA<100° and TR<1500 ms are combined. Previous work reports implementation of HASTE during biopsies with TR=2000 ms [32], which is significantly longer than the minimal TR of 600 ms simulated in this work. Furthermore, during MR-interventions, sequences are repeated for multiple measurements to provide real-time image guidance. Based on contrast measurements on a singular simulation, signal decay and effect on contrast for multiple measurement was not considered and could also influence lesion and tissue to tissue contrast and SNR. Since the current simulation environment is limited in this aspect, validation of the corresponding HASTE sequence, but also the bSSFP sequence at a 3-T MR-system is recommended. For this, the simulated protocols should be executed at the 3-T system with multiple measurements.

For contrast analysis the CNR_{eff} was implemented. Our results showed that the minimal CNR_{eff} of 3-5, as defined by the *Rose Criteria*, is not sufficient for lesion distinction in our simulated case. Based on our experiment, an average of CNR_{eff} 10 was implemented as criterion for lesion distinction. This, however, introduced that the implemented CNR_{eff} does not represent the minimal contrast needed for lesion distinction for all users. Extension of the experiment with more users and more images could provide a better representation of a mean minimal CNR_{eff} for lesion to liver distinction.

A limitation for the determination of the minimal CNR_{eff} was also found in images used during the study. Contrast of lesion to background was decreased by addition of Gaussian noise in the image. This made the latter images in the volume to be excessively noisy and non-representative for images observed during MR-guided interventions. This may have introduced a bias for the clinical readers, in which overall image noise influenced the decision making in which contrast is needed for lesion to background distinction. Alternative images can be introduced, in which contrast of the lesion to its background tissue is lowered by addition of blur, which averages out sudden changes in pixel intensities, and by assigning different signal intensities to the lesion, to provide images more representative for MR-guided interventions.

In conclusion, with implementation of MR-simulations optimal contrast for MR-guided percutaneous interventions was observed for bSSFP and HASTE in the liver. For the bSSFP sequence, FA between 30°-35° are suggested to provide optimal distinction between the lesion and background and tissue to tissue. The influence of FA, and TR were minimal for HASTE suggesting that the lowest FA (100°) and TR (600 ms) can be implemented to provide sufficient distinction. Before clinical implementation, validation of the accurateness of the simulations compared to the MR-environment is required to especially assess SAR limits reached.

Ch. 5

Validation of tissue contrast between MR-phantom experiments and MR-simulations

5.1 Introduction

The previous chapter described the use of MR-simulations to perform sequence optimization for the spoiled GRE, bSSFP and HASTE sequence. The following chapter sets out to answer the second objective of this study, in which tissue contrast from MR-simulations is compared with tissue contrast measurements from a phantom MR-experiment to determine the value of MR-simulations. In order to perform this evaluation, a comparison between a conducted MR-experiment and recreation of this experiment within MR-simulations is performed. As a subobjective, a comparison on the artefact width of a coaxial needle and a cryoablation needle will be executed. The comparison will be used to support the comparison between MR-simulations and the MR-experiment but will also serve as a tool to compare the spoiled GRE, bSSFP and HASTE sequences with one another.

5.2 Method

5.2.1 MRI Phantom Test

For the validation of the simulations a comparison was performed between experimental setup and simulations. Firstly, transversal acquisitions of an abdominal phantom (Model 057A, CIRS, Norfolk) obtained at the 3-T system with *BEAT Interactive* protocols, with GRE and bSSFP contrast, and HASTE protocol were acquired. A 17G nitinol coaxial needle (Innotom, Germany), used during MR-guided biopsies, was positioned in the transversal plane with both a 0° and 40° in-plane angulation. Image acquisition was then repeated. The same process was repeated for a 17G nickel-chromium cryoablation needle (MML Medical, Netherlands).

5.2.2 Materials

Abdominal Phantom model

To perform simulations on a similar model, a 3D-virtual model of the abdominal phantom was made. The acquired HASTE sequence during the MRI phantom test was selected and imported in segmentation software (ITK-SNAP v3.6.0, 2017). A voxel map of the various tissues was created (figure 5.1). The mapped voxel slice was then exported to MATLAB and made into a 3D-voxel map by replication of the slice in the Z-direction. Different models were made with both the coaxial needle and cryoablation needle in the two different angulations.

For needle simulations, a model of the 17G coaxial needle, and a model of the 17G cryoablation needle were created in a CAD program (Solid Edge 2020) (figure 5.1). The needle model was imported as mesh in MATLAB and voxelized to be placed inside the patient model. The needle was placed in the transversal plane with in-plane angulations of 0° and 40° degree to discriminate for needle discretization influences. Although the model was used to represent the needle, different magnetic susceptibility was assigned to either simulate the coaxial needle or the cryoablation needle.

Tissue Characteristics

As input for the simulator, T1- and T2-relaxtion values for the phantom were provided by the manufacturer for 1.4T and obtained by T1- and T2-mapping at 3T. For T1-mapping, the variable flip angle gradient refocused imaging approach described by Fram et al. was used to calculate the T1-

relaxation of the voxels. [35] With this method, the calculation of the T1-relaxation is based on the linear regression between $I(\alpha)/\sin\alpha$ versus $I(\alpha)/\tan\alpha$ which yields a slope determined by $e^{-TR/T1}$. With known TR, the T1-relaxation can be determined from this slope. In the study a T1-VIBE sequence with set TR of 5.2 ms, TE of 2.1 ms and FA's of 2, 5, 10, 15, 20 and 30 were used.

T2-mapping was performed using a multi-SE pulse sequence to sample multiple time points along T2-relaxation decay. TE was sampled thirty-two times with TE variations from 15 ms, till 480 ms (increments of 15 ms) with fixed TR of 2000 ms. A plot of the sampled magnetization will exhibit exponential decay $M_{xy} = M_0 e^{-t/T_2}$. By curve fitting the data points, the T2-relaxation time of the exponential decay was derived. Similar proton density, magnetic susceptibility and chemical shift values as used for the human phantom model were used for the abdominal phantom simulations. For the simulation of the coaxial needle and the cryoablation needle, the magnetic susceptibility of nitinol and nickel-chromium were obtained (appendix A). [36], [37]

5.2.3 MRI simulations

MRI simulations were performed on the same Siemens Bloch-simulator as described in section 4.2.3. Spoiled GRE, bSSFP and HASTE protocols used during the MR-experiment were extracted and imported to the simulator (table 5.2). As input, the abdominal phantom model with either the coaxial or cryoablation needle in the two angulations were used.

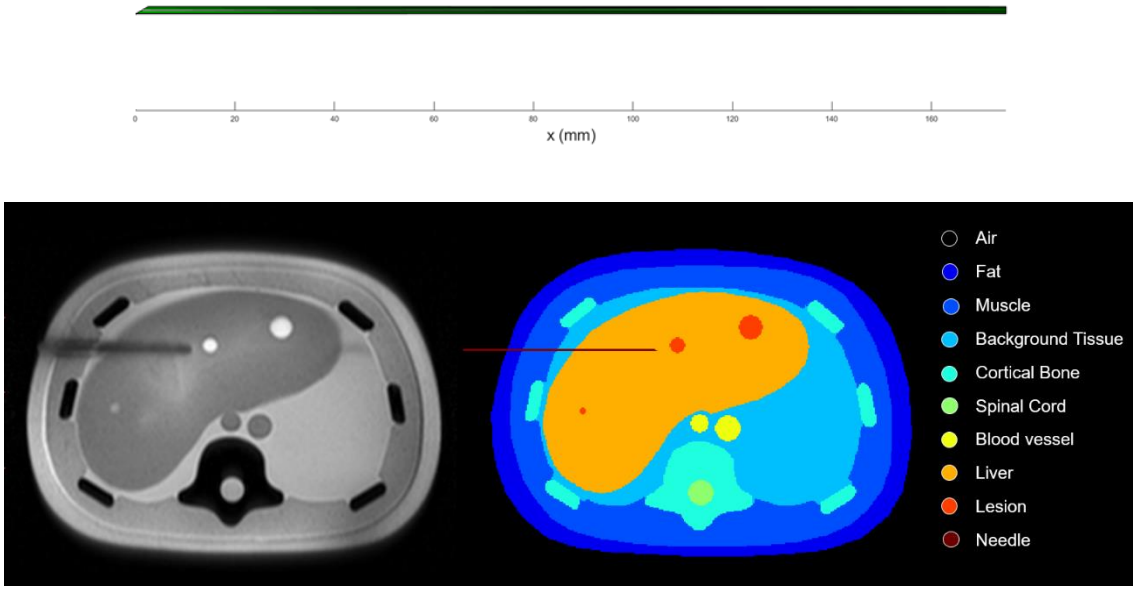

Figure 5.1 - (top) Mesh representation of the 17G needle model representing both the coaxial needle as the cryoablation needle. (bottom) (left) HASTE acquisition of a transversal slice at the level of liver in the abdominal phantom. (right) Transversal slice of the recreated 3D-model, with each colour corresponding to a different material identity (see legend).

5.2.4 Analysis

Contrast comparison between MR-experiment and simulations

Compared to the implemented CNR_{eff} in chapter 4, a different metric was used to compare the lesion and tissue contrasts of the MR-experiment with that of the simulations. This was caused by the spins per voxel parameter for the simulations, which caused large influences on the measured simulated image noise and would therefore influence CNR_{eff}. To avoid bias of the simulated noise, signal ratios relative to the liver were determined between various ROIs. Mean signal was determined by manually selecting ROIs of the lesion, background tissue, muscle, and fat layer in the 3D model. These ROIs were then scaled to fit the images of the MR-experiment and the different simulations. The ratio was determined by dividing the mean intensity of selected ROI with that of the mean liver signal intensity.

Contrast comparison between simulations and signal equations

In an additional step, the signal ratios measured within the simulations were compared with signal ratios determined by solving the spoiled GRE (eq. 3.7) and bSSFP (eq. 3.8) equations. This step was introduced to not only compare the MR-experiment with the simulations, but to verify the agreement of the simulator with the theoretical signal equations. The equations for spoiled GRE and bSSFP were solved with the relaxation times from either the mapping experiment or the manufacturer provided relaxation times, and TR and TE from the corresponding protocols. Resulting signals of the lesion and tissues were then divided by liver signal to determine the signal ratios. Comparison of HASTE with a signal equation was not performed due to the complexity of formulating its signal equation.

Needle width assessment

As a subobjective, needle artefact diameters were compared between the various sequences and between MR-experiment and simulations. Images were loaded in MATLAB. A line along the length of the needle artefact was drawn manually. The image was cropped to sample orthogonal lines of 3 cm between 40-90% of the drawn line along the needle artefact to provide an extensive representation of the artefact. The median of the background tissue along the needle trajectory was determined, and artefact size was segmented by thresholding the image by a 30% increase and decrease in signal intensity, compared to the calculated background signal (ASTM standard F2119-01, [38], [39]). Lastly, the mean width of the segmentation was determined to provide the mean needle diameter.

5.3 Results

5.3.1 T1- and T2-relaxation times of the abdominal phantom model

As input for the tissue parameters for the abdominal phantom model, both the T1- and T2-relaxation values provided by the manufacturer (measured at 1.4-T, simulated at 3-T) and the values resulting from the T1- and T2-mapping experiments (measured at 3-T) were used for simulations. Table 5.1 provides these values. Results show that there is a large difference between the values provided by the manufacturer and the values measured during mapping experiments. Largest differences are found in the measurement of the T1-relaxation. Another striking result is the derived T1- and T2-times of the outer fat layer of the abdomen. Correspondingly, T2-relaxation is longer than T1-relaxation, which is physically not possible.

Table 5.1 - T1 and T2-relaxation values provided by the manufacturer and values derived from the mapping sequences. Great difference in T1- and T2-times is observed. For fat layer, incorrect T1- and or T2-times were measured.

Component	Manufacturer		Mapping Seq.	
Description	T1 (ms)	T2 (ms)	T1 (ms)	T2 (ms)
Liver	1010	86.1	1125	147
Lesion	1800	274.1	1380	553
Background tissue	1350	817	2195	546
Muscle	920	181.6	1342	354
Fat Layer	270	234	20	87

5.3.2 Contrast comparison between MR-experiment and simulations

In total 12 sequences were performed at the MR-system on the abdominal phantom. Accordingly, these 12 measurements were identically repeated with the Bloch-simulator for image comparison. The sequence settings used are stated in table 5.2. Slight adjustments had to be made during the simulations to successfully run the sequence protocols. For the spoiled GRE sequence, one additional measurement was simulated (TR=606 ms, Acq. Matrix=162x1600) and for the bSSFP sequence, TR was lowered to 391 ms. To lower computational time for the simulations, the ten initial measurements were lowered to four. During the comparison, the fourth slice of the MR-acquisition was used.

Table 5.2 – Sequence parameters for the spoiled GRE, bSSFP and HASTE protocols used during the abdominal phantom MR-experiment. Parameters include echo time (TE), repetition time (TR), echo spacing (ES), flip angle (FA), field-of-view (FOV), acquisition (Acq) matrix, partial Fourier sampling, measurements (Meas.) and acquisition time (AT).

Sequence	TE/TR (ms)	ES (ms)	FA (°)	FOV (mm)	Acq Matrix	Partial Fourier	Meas.	AT (s)
GRE	2.4 / 601	4.5	15	300x300	161x160	6/8	10	6
bSSFP	1.5 / 398	2.9	35	300x300	160x160	6/8	10	4
HASTE	53 / 600	5.3	136	307x250	192x126	5/8	10	6

Comparison of the spoiled GRE sequence

Figure 5.2 shows the results of the spoiled GRE MR-experiment, simulation with T1- and T2-mapped tissue values and the simulation with manufacturer provided tissue values. Window levels are visually adjusted to match signal intensities with the background tissue. Upon visible comparison, large differences in contrast are visible between the MR-experiment and simulations.

Signal ratios relative to liver were measured for lesion, background tissue, muscle and fat and supported the visual observation of disagreement in contrasts. (table 5.3) With exception of the signal ratio of lesion in the manufacturer simulation, all signal ratios of both simulations showed increased signal ratios compared to the MR-experiment. Most noticeable is the large difference in the outer fat signal withing the simulation with mapping input, which is 7 times as bright as liver signal in the mapping simulation. This finding is attributed to the low mapped T1- and T2-times of the fat layer.

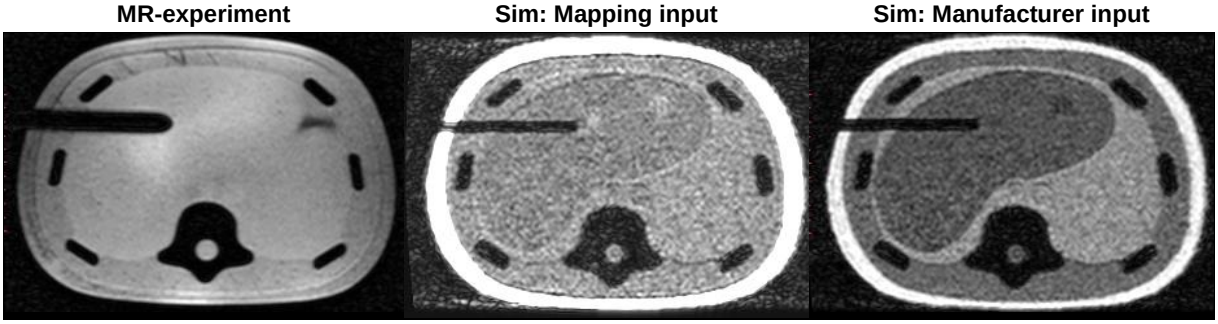

Figure 5.2 – Results for the GRE sequence for MR-experiment, simulation (Sim) with the mapping T1- T2-times and the simulation with manufacturer provided T1- T2-times. Large differences in contrast are visually observed.

Table 5.3 – Signal ratios relative to liver for lesion, background tissue, muscle and fat in both the simulation with the mapping T1- T2-times and the simulation with manufacturer T1- T2-times, show increased ratios compared to the MR-experiment. Signal of the fat layer in the sim with mapping inputs showed a signal ratio of 7.1, caused by the implemented T1- and T2-times.

Signal ratios (relative to liver signal)	MR-experiment	Sim: Mapping input	Sim: Manufacturer input
Lesion	1.1	1.3	0.7
Background tissue	0.9	1.2	1.8
Muscle	0.7	1.1	1.2
Fat	0.7	7.1	2.9

Comparison of the bSSFP sequence

Figure 5.3 shows the results of the bSSFP MR-experiment, simulation with T1- and T2-mapped tissue values and the simulation with manufacturer provided tissue values. Similar to the spoiled GRE results, lack of similarity is observed. Measured signal ratios support visual observation and show for both the simulations a strong increase in contrast (>factor 1.4) (table 5.4). In both simulations, liver appears to have a lower signal intensity compared to the MR-experiment, contributing to higher signal ratios for the various tissues.

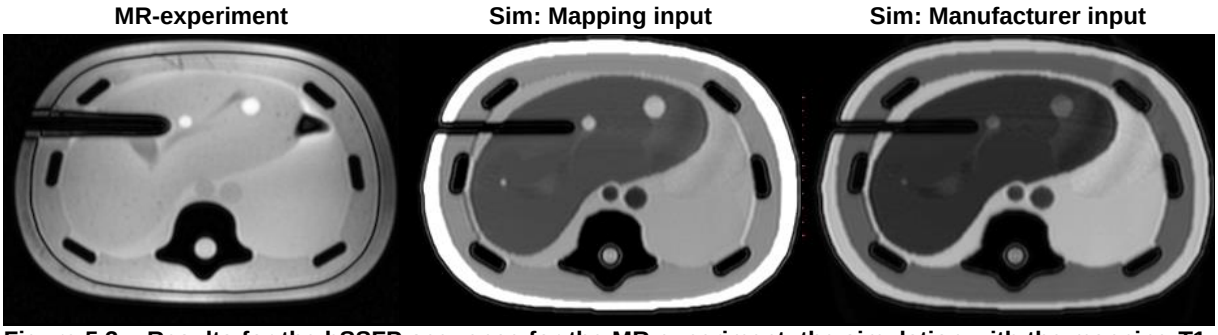

Figure 5.3 – Results for the bSSFP sequence for the MR-experiment, the simulation with the mapping T1- T2-times, and the simulation with manufacturer provided T1- T2-times. Lack of similarity between the MR-experiment and the simulations is visually observed in which liver shows specifically low sign

Table 5.4 – Calculated bSSFP signal ratios relative to liver for lesion, background tissue, muscle and fat in the MR-experiment, simulation with the mapping T1- T2-times and the simulation with manufacturer T1- T2-times. Lack of similarity is supported by the higher signal ratios for both simulations. Strongest signal ratios were measured for fat (4.2) in both simulations and background tissue (4.0) for the simulation with manufacturer input.

Signal ratios (relative to liver signal)	MR-experiment	Sim: Mapping input	Sim: Manufacturer input
Lesion	1.5	2.3	2.1
Background tissue	1.0	2.0	4.0
Muscle	0.7	1.8	2.1
Fat	0.6	4.2	4.2

Comparison of the HASTE sequence

Figure 5.4 presents the HASTE images of the MR-experiment and the two different simulations. Comparison between the HASTE MR-experiment and the simulations show no visible agreement. An interesting finding is the appearance of the fat layer in the simulation with mapped T1- and T2-relaxation times. This showed throughout a speckling pattern, which is probably introduced to the T1- and T2-measurements of the fat layer (table 5.1). The measured signal ratios support the lack of agreement in contrasts and are noted in table 5.5.

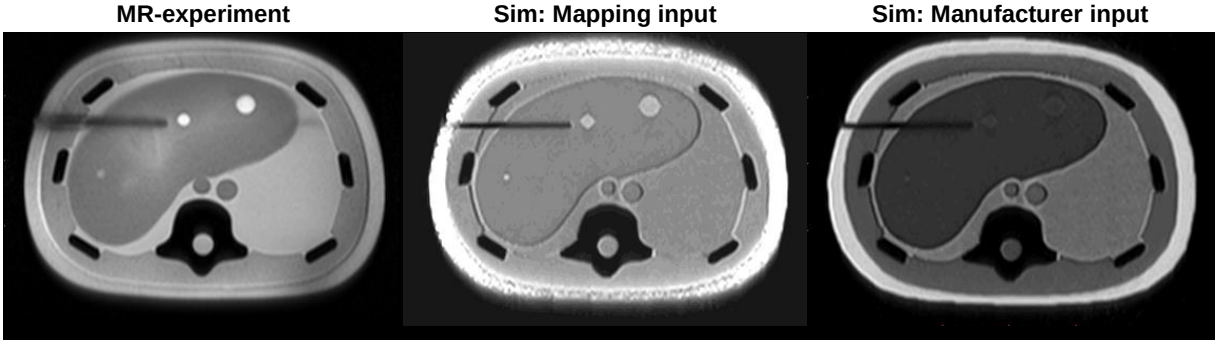

Figure 5.4 - Results for the HASTE sequence for the MR-experiment, the simulation with the mapping T1- T2-times and the simulation with provided T1- T2-times. Simulations show different appearance compared to the MR-experiment. A speckling pattern is observed for the fat layer in the simulation with mapping input, caused by the implemented T1- and T2-relaxation times.

Table 5.5 – Calculated HASTE signal ratios relative to liver for lesion, background tissue, muscle and fat in the MR-experiment, simulation (with the mapping T1- T2-times and the simulation with manufacturer T1- T2-times. Signal ratios of the simulations show lack of agreement compared to the MR-experiment.

Signal ratios (relative to liver signal)	MR-experiment	Sim: Mapping input	Sim: Manufacturer input
Lesion	1.9	1.4	1.1
Background tissue	1.4	1.0	2.0
Muscle	0.9	1.2	1.6
Fat	1.3	2.5	4.0

5.3.3 Contrast comparison between simulations and signal equations

Within the comparison between the MR-experiment and the simulations, overall lack of agreement was observed. To further verify the results of the simulations, a comparison between the measured signal ratios from the simulations with signal ratios determined by the signal equations of the spoiled GRE (eq. 3.7) and bSSFP (eq. 3.8) was performed. Figure 5.5 provides the relative difference in derived signal ratios between the simulations and signal equations for both mapping and manufacturer provided T1- and T2-times.

The results illustrate that overall higher signal ratios were determined within the simulations compared to the sequence equations (relative difference>1). The relative difference in signal ratios between the spoiled GRE simulations was lower compared to the bSSFP simulations. The results therefore suggest that the Bloch-simulator provides similar magnetization behaviour compared to the spoiled GRE equation for corresponding input. Lower correspondence is observed between the Bloch-simulator and the bSSFP equation.

Between the two different T1- and T2-inputs (mapping and manufacturer), no great differences were observed. This was expected since the inputs between the simulations and the sequence equations were matched for the different T1- and T2-inputs.

Figure 5.5 – Relative difference in signal ratios (relative to liver) of lesion, background (bgr) tissue, muscle, and fat between the simulations and signal equations for the spoiled GRE (left) and bSSFP (right) sequences, for both mapping (blue) and manufacturer (light blue) T1- and T2-inputs. For the spoiled GRE, relative differences between simulations and signal equations for lesion, muscle and fat were low: 1.5, 1.2 and 0.8 for the mapping input and 1.2, 1.1 and 1.0 for the manufacturer input. For bSSFP, the relative difference in signal ratios exceeded 1.4 for all measurements.

5.3.4 Needle Diameters

As a subobjective within this study, a comparison of the needle diameters was performed between the MR-experiment and the simulation, the three different sequences and the two different needles. Figure 5.6 presents the measured widths of the needle artefacts.

During the MR-experiment, largest artefacts were found for the bSSFP sequence (coaxial needle: 19 mm, cryoablation needle: 15 mm) followed by the spoiled GRE (coaxial needle: 17 mm, cryoablation needle: 14 mm) and concluded by HASTE (coaxial needle: 5 mm, cryoablation needle: 6 mm)

Figure 5.7 illustrates both underestimation of the needle artefact for spoiled GRE and bSSFP simulations compared to the MR-experiment. Greatest differences were measured for the coaxial needle: for both spoiled GRE and bSSFP, average of 8 mm difference between MR-experiment and simulations. Differences in cryoablation artefact width were lower compared to the coaxial needle: for spoiled GRE, average of 4 mm difference between MR-experiment and simulations, for bSSFP, average of 3 mm difference between MR-experiment and simulations. The results indicate difference in true magnetic susceptibility and modelled susceptibility and, or difference in simulated T2-star weighting compared to the MR-findings.

Simulations of the HASTE sequence showed closer similarity to the MR-experiment. Deviation between the mean width of the coaxial needle was small (simulated width of 5 mm versus MR-experiment width of 6 mm). For the cryoablation needle no difference was measured (both 6 mm). Due to the lower influence of magnetic susceptibility differences within this sequence, stronger agreement is observed for HASTE than the spoiled GRE and bSSFP sequences.

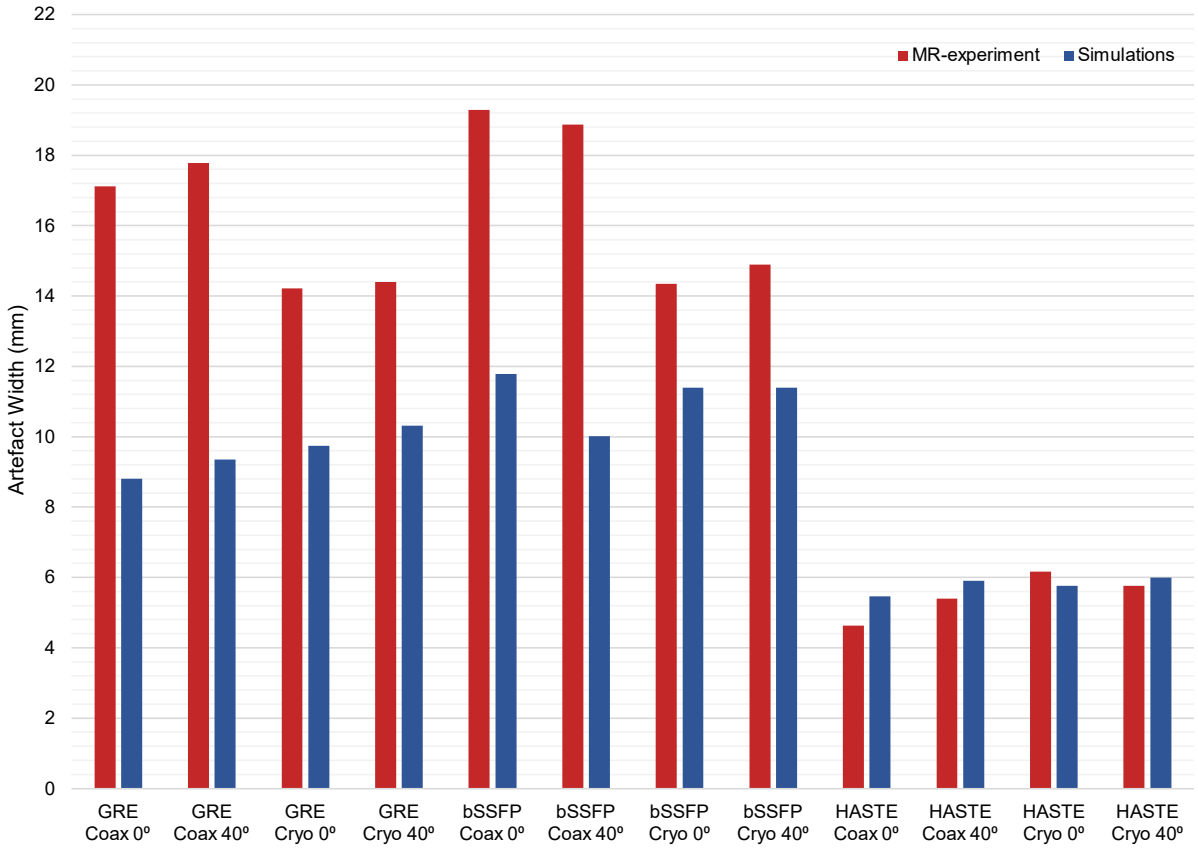

Figure 5.6 - Measured needle diameters (artefact width) of the coaxial needle and the cryoablation needle during the MR-experiment and simulations of the spoiled GRE, bSSFP and HASTE sequences with transversal in-plane angulations of 0° and 40°. Large deviations are observed for both the spoiled GRE and bSSFP needle artefacts. Needle artefact width is in correspondence for the HASTE sequence.

5.4 Discussion

Chapter 5 described the validation of tissue contrast between MR-phantom experiment and MR-simulations. The use and implementation of MR-simulations has extensively been reported, with applications such as sequence optimization [16], understanding of artefacts [18], [19] and training AI-algorithms for needle tracking [20]. The Siemens MR-simulator is based on the work of Stöcker et al. [27] and provides a tool for realistic MR-simulations in which Bloch-equations are solved for a particular sequence on a voxel-based model with multiple tissue characteristics such as relaxation time and magnetic susceptibility. The work presented, however, showed that there are still large visible as quantitative deviations in contrast between the simulations and the MR-measurements. Based on the results found during this study, it can be concluded that there was no useful comparison found between MR-experiments and simulations in our current work. There are various aspects that have contributed to this deviation that will help to understand the reported disagreement between MR-simulations and the MR-experiment and will aid in optimization of MR-simulations in future work.

A large contribution to the differences between the MR-experiment and the simulations can be accounted to the abdominal model inputs such as relaxation times. During this study, phantom tissue properties were determined by the manufacturer and by T1- and T2-mapping experiments. Comparison between the measurements showed a large difference between provided values and measured values.

These differences can both be attributed to difference in field strength, deterioration of the phantom model but also difference in T1- and T2-mapping techniques. For instance, the work of Stikov et al. compared the Look-Locker and variable flip angle T1-mapping methods with the inversion recovery method as gold standard. Results showed that for both phantom measurements as in vivo measurements, the variable flip angle method overestimated T1-relaxation times with 30% compared to the gold standard. [40] For the fat layer, a T1- and T2-relaxation time of 20 and 87 ms was measured. Since the T1-time is physically always greater than T2-time, this finding indicates that either the mapping techniques, or calculation of the tissue times, showed errors. As improvement, different T1- and T2-mapping sequences should be used to compare if the findings are related to the sequence, or the calculation approach. For future validation, it is recommended to also introduce validation on a calibrated phantom with known T1- and T2-times in order to assess the applied mapping techniques and calculation methods.

A second input related effect that caused deviations in contrast is that of the voxel representation of the abdominal model itself. In this experiment, a HASTE acquisition of the abdominal phantom was used to create a segmentation map of the 3D model. The segmentation map was then used to assign tissue intrinsic values. The pitfall of this approach is that intrinsic tissue value allocation was based on distinctive borders and tissues of a T2-weighted image. When compared to the T1-map, a less distinctive image was observed. This possibly contributes to differences in tissue discrimination in the T1-weighted GRE and T1/T2 weighted bSSFP images.

Besides input related effects, deviations between the simulations and the MR-experiment can also be attributed to simulator related effects. Within this work, a comparison between signal ratios from the Bloch-simulator and the sequence equations was introduced to observe the correspondence in solving the magnetization dynamics on the implemented model. While spoiled GRE showed low relative differences in signal ratios, bSSFP simulations showed relative difference greater than 1.4 compared to its sequence equation, indicating differences in magnetization behaviour between the simulator and theoretical signal. Relative chances can be explained by two principles. Both the sequence equations of spoiled GRE and bSSFP describe the signal intensity within a steady state. Deviations between the signal ratios measured within the simulations, and signal ratios determined by the sequence equations may suggest that within the simulated image, no steady state was yet achieved. Furthermore, the Bloch-simulator also accounts for variables such as noise and susceptibility, which cannot be implemented within the sequence equations, and may have also contributed to the observed deviations.

While the Bloch-simulator implements magnetic susceptibility to introduce field-inhomogeneities, the lack of agreement between simulations and MR-experiment indicates difficulty to create a realistic perturbation in the homogeneous B0-field. During an MR-experiment, there are multiple external influences that introduce these deviations such as the scanner and its hardware, motion, or tissue composition. These deviations lead to T2-star relaxation and certain artefacts. Simulations could therefore be improved by also simulating the influence of these external factors on the perturbation of the homogenous B0-field.

The final results of this work described comparison between the needle artefact widths. Once more, disagreement between the MR-experiment and simulations was observed. Similarly, to the abdominal phantom, deviations can largely be explained by the assigned input (magnetic susceptibility) and the implemented needle model. In other works, the magnetic susceptibility (χ) of the needle is assigned with the magnetic susceptibly of titanium (χ=182 ppm) [19]. In this work, χ of 245 ppm for the coaxial needle and χ of 350 ppm for the cryoablation were used. Although a greater difference in magnetic susceptibility was used compared to other work, the reported differences between simulation and MR-experiment in needle artefact width were still significantly smaller. [19] Great differences in needle width were mainly measured for the GRE and bSSFP sequence. Both these sequences do not rephase intravoxel dephasing, making them more susceptible to the difference in magnetic susceptibility. No significant differences were observed for the HASTE, which does rephase intravoxel dephasing. This further indicates that the magnetic susceptibility implemented is possibly incorrect and needs further

optimization. Since the device manufactures do not share the exact compositions of the used alloys, additional measurements need to be performed to get more accurate magnetic susceptibility values.

Limitations in the needle modelling were also present. This was mainly caused by the maximum resolution of 2 pixels/mm for the abdominal model. Since the diameter of the needle is 1.5 mm, solely 3 pixels could be used for needle width, introducing discretization issues. As intravoxel dephasing is bound to the image resolution, a decrease in the true susceptibility field around the needle and its surroundings is introduced for lower resolutions. For future needle modelling, modelling with higher resolutions could solve this issue and better represent the influence of the needle on the main magnetic field. This would require increased computational power to limit extensive increase in simulation time.

In general, both improvements in the model inputs, as improvements in recreation of the inhomogeneous B0-field during MR-experiments should be implemented to further establish the accuracy of MR-simulations. With inputs being improved, the potential of realistic MR-simulations can increase, further aiding potential applications such as sequence optimization. If the current limitations found in this work are addressed, it is expected that accurate MR-simulations can be provided and will have more clinical relevance.

Ch. 6

General Discussion, Outcomes and Future Perspectives

The goal of this thesis was to optimize real-time MR-guided needle interventions with the use of MR-simulations. Within this work, first steps are conducted in the implementation of MR-simulations within the field of interventional MRI. In the first objective of this study, tissue contrast optimization was performed by varying various parameters for the spoiled GRE, bSSFP and HASTE sequence. Subsequently the second objective of this study was to validate the tissue contrast between MR-phantom experiments and MR-simulations. Based on the combination of the outcome of both objectives, the following remarks can be made regarding the main goal: *Optimization of real-time MR-guided needle interventions with the use of MR-simulations.*

Foremost, due to the observed disagreement between the MR-experiments and MR-simulations in chapter 5, this thesis lacks the results to provide recommendations for direct clinical implementation. The reported results, however, do provide guidance to further improve the use of MR-simulations within the field of MRI-guided percutaneous interventions.

Regarding the results, an understanding of potential variations within sequence settings for MR-guided interventions for the clinician is obtained. While these findings are still unsubstantiated for clinical implementation, they do serve as a foundation for further optimization. The current findings suggest feasible contrast with bSSFP with FA's between 30°-35°, and HASTE with lowest simulated TR of 600 ms and FA of 100°, while framerates of 1 Hz are achieved. Within the subobjective in chapter 5, the different needle artefacts for all sequences were shown, in which largest artefacts were observed for bSSFP, followed by spoiled GRE, and concluded with HASTE. Based on these findings, HASTE is suggested as optimal sequence, followed by bSSFP, and then spoiled GRE.

As MR-simulations in this work showed inaccurate representation of the MR-environment, it is necessary to validate the image contrasts on a patient or healthy volunteer in a MR-scanner. Repeated measurements should be performed to investigate the influence on image contrast and signal to noise within the sequences. Secondly, it is suggested to measure the limits of HASTE with respect to minimal framerate within a MR-environment on a human patient, to make sure SAR limits are not reached during intervention.

To further improve the application of MR-simulations for sequence optimization, future work should specifically focus on optimization of model inputs, in which the tissue characteristics should be matched between MR-experiment and simulations to facilitate accurate model comparison between MR-acquisition and MR-simulation. For instance, comparison between MR-experiment and MR-simulations for phantoms with pre-known T1- and T2-times should be implemented to provide evidence in the accuracy of the simulated tissue contrasts. This work can then be extended with experiments to compare the needle artefact and find the corresponding magnetic susceptibility. Additionally, needle modelling with higher resolutions should be performed to improve the influence on change in magnetic susceptibility on neighboring voxels. Further improvements for accurate MR-simulations also involve the Bloch-simulator. Optional external factors to influence the B0-homogeniteity should be modeled to provide a more similar environment as within the MR-scanner.

Lastly, when the agreement between MR-simulations and MR-experiments is optimized, the current model should be extended to other applications. Since MR-guided percutaneous interventions encompass treatment for various malignancies, extrapolation of the results for other organs and corresponding lesions should be performed. The distinction of lesion to liver background is mainly

influenced by the differences in T1- and T2-times. To extent the recommendations for broader purposes, T1- and T2-times of other tissues and corresponding malignancies such as renal and renal cell carcinoma should be implemented.

In conclusion, limitations in MR-simulations are still present, which cause that the observed sequences and sequence settings cannot directly be implemented in clinical routine. However, within this work, various limitations were observed that could provide insight to improve the potential of MR-simulations for sequence optimization. It is expected that, when mentioned limitations are overcome, MR-simulations could still provide various advantages. For the clinician, simulations could aid in providing contrast information on patient specific cases, substituting MR-phantoms with non-specific anatomy. For the researcher, simulations could provide a tool to acquire clinical realistic images for experimentation with sequence optimization or provide patient accurate training data for implementation in AI-algorithms.

References

[1] C. M. Moore *et al.*, “Image-Guided Prostate Biopsy Using Magnetic Resonance Imaging–Derived Targets: A Systematic Review,” *Eur. Urol.*, vol. 63, no. 1, pp. 125–140, 2013.

[2] M. Maybody, “An overview of image-guided percutaneous ablation of renal tumors,” *Semin. Intervent. Radiol.*, vol. 27, no. 3, pp. 261–267, 2010.

[3] J. M. Llovet and J. Bruix, “Novel advancements in the management of hepatocellular carcinoma in 2008,” *Journal of Hepatology*, vol. 48, no. SUPPL. 1. J Hepatol, 2008.

[4] F. Ridouani and G. Srimathveeravalli, “Percutaneous image-guided ablation: From techniques to treatments,” *Presse Med.*, vol. 48, no. 7, Part 2, pp. e219–e231, 2019.

[5] H. S. Kim, J. Chapiro, and J. F. H. Geschwind, “From the Guest Editor: Interventional Oncology: The Fourth Pillar of Oncology,” *Cancer Journal (United States)*, vol. 22, no. 6. Lippincott Williams and Wilkins, pp. 363–364, 2016.

[6] E. Rothgang, W. D. Gilson, F. Wacker, J. Hornegger, C. H. Lorenz, and C. R. Weiss, “Rapid freehand MR-guided percutaneous needle interventions: An image-based approach to improve workflow and feasibility,” *J. Magn. Reson. Imaging*, vol. 37, no. 5, pp. 1202–1212, May 2013.

[7] J. P. Kühn *et al.*, “Magnetic resonance-guided upper abdominal biopsies in a high-field wide-bore 3-T MRI system: Feasibility, handling, and needle artefacts,” *Eur. Radiol.*, vol. 20, no. 10, pp. 2414–2421, 2010.

[8] M. Moche *et al.*, “Navigated MRI-guided liver biopsies in a closed-bore scanner: experience in 52 patients,” *Eur. Radiol.*, vol. 26, no. 8, pp. 2462–2470, 2016.

[9] P. de Marini *et al.*, “Percutaneous MR-guided prostate cancer cryoablation technical updates and literature review,” *BJR|Open*, vol. 1, no. 1, p. 20180043, 2019.

[10] S. K. Bhagavatula, K. Tuncali, P. B. Shyn, V. M. Levesque, S. L. Chang, and S. G. Silverman, “Percutaneous CT- And MRI-guided cryoablation of CT1 renal cell carcinoma: Intermediate- And long-term outcomes in 307 patients,” *Radiology*, vol. 296, no. 3, pp. 687–695, 2020.

[11] E. A. Kaye, K. L. Granlund, E. A. Morris, M. Maybody, and S. B. Solomon, “Closed-Bore Interventional MRI: Percutaneous Biopsies and Ablations,” *Am. J. Roentgenol.*, vol. 205, no. 4, pp. W400–W410, Oct. 2015.

[12] A. E. Campbell-Washburn, A. Z. Faranesh, R. J. Lederman, and M. S. Hansen, “Magnetic Resonance Sequences and Rapid Acquisition for MR-Guided Interventions,” *Magnetic Resonance Imaging Clinics of North America*, vol. 23, no. 4. W.B. Saunders, pp. 669–679, 01-Nov-2015.

[13] J. L. Duerk, E. Y. Wong, and J. S. Lewin, “A brief review of hardware for catheter tracking in magnetic resonance imaging,” *Magma Magn. Reson. Mater. Physics, Biol. Med.*, vol. 13, no. 3, pp. 199–208, Oct. 2001.

[14] S. R. Yutzy and J. L. Duerk, “Pulse sequences and system interfaces for interventional and real-time MRI,” *Journal of Magnetic Resonance Imaging*, vol. 27, no. 2. pp. 267–275, Feb-2008.

[15] F. Liu, J. V Velikina, W. F. Block, R. Kijowski, and A. A. Samsonov, “Fast Realistic MRI Simulations Based on Generalized Multi-Pool Exchange Tissue Model,” *IEEE Trans. Med. Imaging*, vol. 36, no. 2, pp. 527–537, 2017.

[16] G. Andria, F. Attivissimo, G. Cavone, and A. M. L. Lanzolla, “Acquisition times in magnetic resonance imaging: Optimization in clinical use,” *IEEE Trans. Instrum. Meas.*, vol. 58, no. 9, pp. 3140–3148, 2009.

[17] L. G. Hanson, “A Graphical Simulator for Teaching Basic and Advanced MR Imaging Techniques,” *RadioGraphics*, vol. 27, no. 6, pp. e27–e27, 2007.

[18] C. A. Cocosco, V. Kollokian, R. K. Kwan, G. B. Pike, and A. C. Evans, “BrainWeb: Online Interface to a 3D MRI Simulated Brain Database.” .

[19] E. Beld, M. A. Moerland, J. R. N. V. D. V. Van Zyp, M. A. Viergever, J. J. W. Lagendijk, and P. R. Seevinck, “MRI artifact simulation for clinically relevant MRI sequences for guidance of prostate HDR brachytherapy,” *Phys. Med. Biol.*, vol. 64, no. 9, 2019.

[20] R. Uhlig, “Deep Learning based Passive Needle Tracking for MR-Guided Percutaneous Interventions Optimized with Synthetic Data,” [Unpublished master’s thesis] Friedrich-Alexander-Universität Erlangen-Nürnberg, 2020.

[21] G. Brix *et al.*, “Basics of Magnetic Resonance Imaging and Magnetic Resonance Spectroscopy,” *Magnetic Resonance Tomography*. Springer Berlin Heidelberg, pp. 3–167, 2008.

[22] F. Bloch, “Nuclear induction,” *Phys. Rev.*, vol. 70, no. 7–8, pp. 460–474, 1946.

[23] K. Butts, J. M. Pauly, B. L. Daniel, S. Kee, and A. M. Norbash, “Management of biopsy needle artifacts: Techniques for RF-refocused MRI,” *J. Magn. Reson. Imaging*, vol. 9, no. 4, pp. 586–595, 1999.

[24] J. D. Port and M. G. Pomper, “Quantification and minimization of magnetic susceptibility artifacts on GRE images,” *J. Comput. Assist. Tomogr.*, vol. 24, no. 6, pp. 958–964, 2000.

[25] A. Haase, J. Frahm, D. Matthaei, W. Hanicke, and K.-D. Merboldt, “FLASH imaging. Rapid NMR imaging using low flip-angle pulses,” *J. Magn. Reson.*, vol. 67, no. 2, pp. 258–266, 1986.

[26] K. Scheffler, “On the transient phase of balanced SSFP sequences,” *Magn. Reson. Med.*, vol. 49, no. 4, pp. 781–783, 2003.

[27] T. Stöcker, K. Vahedipour, D. Pflugfelder, and N. J. Shah, “High-performance computing MRI simulations,”

Magn. Reson. Med., vol. 64, no. 1, pp. 186–193, 2010.
[28] R. E. Hendrick, “Signal, Noise, Signal-to-Noise, and Contrast-to-Noise Ratios,” *Breast MRI*. Springer New York, pp. 93–111, 2008.
[29] J. W. Massey and A. E. Yilmaz, “AustinMan and AustinWoman: High-fidelity, anatomical voxel models developed from the VHP color images,” in *Proceedings of the Annual International Conference of the IEEE Engineering in Medicine and Biology Society, EMBS*, 2016, vol. 2016-Octob, pp. 3346–3349.
[30] S. W. Farraher, H. Jara, K. J. Chang, A. Ozonoff, and J. A. Soto, “Differentiation of hepatocellular carcinoma and hepatic metastasis from cysts and hemangiomas with calculated T2 relaxation times and the T1/T2 relaxation times ratio,” *J. Magn. Reson. Imaging*, vol. 24, no. 6, pp. 1333–1341, 2006.
[31] P. A. Bottomley, T. H. Foster, R. E. Argersinger, and L. M. Pfeifer, “A review of normal tissue hydrogen NMR relaxation times and relaxation mechanisms from 1â□“100 MHz: Dependence on tissue type, NMR frequency, temperature, species, excision, and age,” *Med. Phys.*, vol. 11, no. 4, pp. 425–448, 1984.
[32] J. Stattaus, S. Maderwald, M. Forsting, J. Barkhausen, and M. E. Ladd, “MR-guided core biopsy with MR fluoroscopy using a short, wide-bore 1.5-Tesla scanner: Feasibility and initial results,” *J. Magn. Reson. Imaging*, vol. 27, no. 5, pp. 1181–1187, 2008.
[33] H. Rempp *et al.*, “Liver lesion conspicuity during real-time MR-guided radiofrequency applicator placement using spoiled gradient echo and balanced steady-state free precession imaging,” *J. Magn. Reson. Imaging*, vol. 40, no. 2, pp. 432–439, 2014.
[34] A. Deshmane, V. Gulani, M. A. Griswold, and N. Seiberlich, “Parallel MR imaging,” *Journal of Magnetic Resonance Imaging*, vol. 36, no. 1. John Wiley & Sons, Ltd, pp. 55–72, 2012.
[35] E. K. Fram *et al.*, “Rapid calculation of T1 using variable flip angle gradient refocused imaging,” *Magn. Reson. Imaging*, vol. 5, no. 3, pp. 201–208, 1987.
[36] C. Shi *et al.*, “Positive visualization of MR-compatible nitinol stent using a susceptibility-based imaging technique,” *Quant. Imaging Med. Surg.*, vol. 9, no. 3, pp. 477–490, 2019.
[37] J. Starčuková, Z. Starčuk, H. Hubálková, and I. Linetskiy, “Magnetic susceptibility and electrical conductivity of metallic dental materials and their impact on MR imaging artifacts,” *Dent. Mater.*, vol. 24, no. 6, pp. 715–723, 2008.
[38] “ASTM F2119 - Standard Test Method for Evaluation of MR Image Artifacts from Passive Implants | Engineering360.” .
[39] T. O. Woods, “Standards for medical devices in MRI: Present and future,” *J. Magn. Reson. Imaging*, vol. 26, no. 5, pp. 1186–1189, 2007.
[40] N. Stikov, M. Boudreau, I. R. Levesque, C. L. Tardif, J. K. Barral, and G. B. Pike, “On the accuracy of T1 mapping: Searching for common ground,” *Magn. Reson. Med.*, vol. 73, no. 2, pp. 514–522, 2015.
[41] J. F. Schenck, “The role of magnetic susceptibility in magnetic resonance imaging: MRI magnetic compatibility of the first and second kinds,” *Med. Phys.*, vol. 23, no. 6, pp. 815–850, 1996.
[42] I. Foundation, “Tissue Properties Database V4.0,” 2018.
[43] F. A. Duck, “Chapter 9 - Tissue Composition,” *Physical Properties of Tissues*. Academic Press, pp. 319–328, 1990.
[44] J. Du *et al.*, “Assessment of cortical bone with clinical and ultrashort echo time sequences,” *Magn. Reson. Med.*, vol. 70, no. 3, pp. 697–704, 2013.
[45] M. N. Hood, V. B. Ho, J. G. Smirniotopoulos, and J. Szumowski, “Chemical shift: The artifact and clinical tool revisited,” *Radiographics*, vol. 19, no. 2, pp. 357–371, 1999.
[46] S. Richard *et al.*, “In vivo proton relaxation times analysis of the skin layers by magnetic resonance imaging,” *J. Invest. Dermatol.*, vol. 97, no. 1, pp. 120–125, 1991.

Appendices

A1 Model tissue parameters

Tissue [A]	Material ID	T1-relaxation (ms)	T2-relaxation (ms)	Proton Density (^1H density) ($kg^{-1} \times 10^{25}$)	Magnetic Susceptibilty (10^{-6})	Chemical Shift frequency (hz)
Air External	0	-	-	-	0.3 [41]	0
Aorta	20	1984 [42]	275 [42]	3.38 [43]	-7.9 [41]	0
Blood Vessel	28	1984 [42]	275 [42]	3.27 [43]	-7.9 [41]	0
Bone Cortical	84	230 [44]	1 [44]	1.05 [43]	-8.9 [41]	0
Bone Marrow	92	586 [42]	49 [42]	3.60 [43]	-9.0 [41]	0
Cartilage	112	1201 [42]	44 [42]	3.16 [43]	-9.0 [41]	0
Colon	4	650 [4]	60 [4]	3.52 [43]	-9.0 [41]	0
Colon Internal	6	650 [4]	60 [4]	3.52 [43]	-9.0 [41]	0
DCT	219	500 [43]	5 [43]	3.56 [43]	-9.0 [41]	0
Diaphragm	181	1233 [42]	37 [42]	3.38 [43]	-9.0 [41]	0
Esophagus	144	800 [31]	60 [31]	3.45 [43]	-9.0 [41]	0
Fat	136	377 [41]	98 [42]	3.82 [43]	-9.0 [41]	-430 [45]
Liver	108	810 [41]	38 [41]	3.38 [43]	-9.0 [41]	0
Lung Inflated	128	1000 [31]	95 [31]	1.05 [43]	0.3 [41]	0
Muscle	180	1233 [41]	37 [41]	3.38 [43]	-9.0 [41]	0
Nerve	192	1083 [41]	78 [41]	3.56 [43]	-9.0 [41]	0
Skin	204	620 [46]	30 [46]	3.31 [43]	-9.0 [41]	0
Spinal Cord	184	993 [41]	78 [41]	3.56 [43]	-9.0 [41]	0
Spinal Fluid	80	4000 [43]	2000 [43]	3.71 [43]	-9.0 [41]	0
Spleen	188	1328 [41]	61 [41]	3.41 [43]	-9.0 [41]	0
Stomach	200	765 [31]	60 [31]	3.45 [43]	-9.0 [41]	0
Stomach Internal	201	765 [31]	60 [31]	3.45 [43]	-9.0 [41]	0
Tendon	220	500 [43]	5 [43]	3.56 [43]	-9.0 [41]	0
Lesion – 3 mm	50	760 [30],[31]	83 [30],[31]	3.38 [43]	-9.0 [41]	0
Lesion – 5 mm	51	760 [30],[31]	83 [30],[31]	3.38 [43]	-9.0 [41]	0
Lesion – 10 mm	52	760 [30],[31]	83 [30],[31]	3.38 [43]	-9.0 [41]	0
Lesion – 15 mm	53	760 [30],[31]	83 [30],[31]	3.38 [43]	-9.0 [41]	0
Lesion – 20 mm	54	760 [30],[31]	83 [30],[31]	3.38 [43]	-9.0 [41]	0
Needle – Coax	70	-	-	-	245 [36]	0
Needle – Cryo	71	-	-	-	350 [37]	0

A2 Supplementary Figures

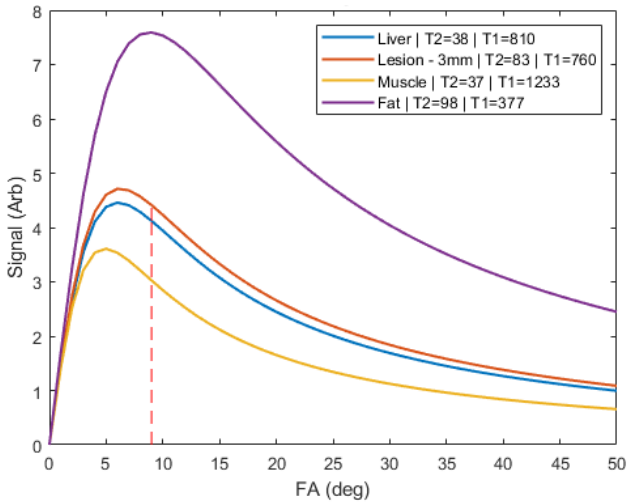

Figure A2.1 - Theoretical signal of the GRE contrast between FA's 0-50° with TR=4.5 ms and TE=2.44 ms, for liver, lesion muscle and fat. Implemented T1- and T2-values are provided in the legend. No large contrast difference is found during the FA variations between liver and lesion. Highest signal intensities were found between FA=5° and approximately FA=30°, at corresponding TR and TE values. The highest difference in signal between liver and lesion is found at FA=9°.

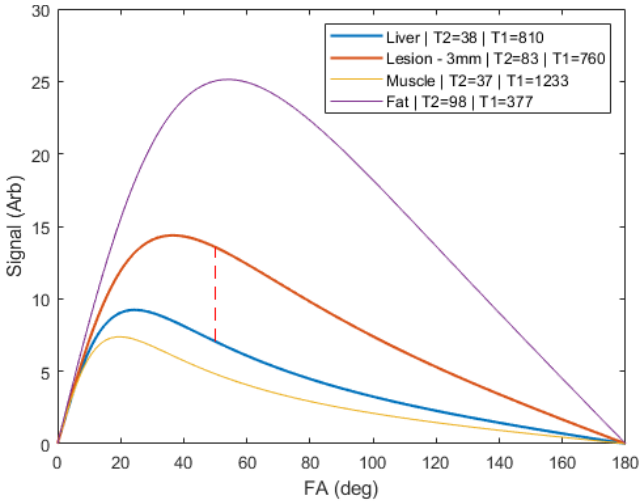

Figure A2.2 - Theoretical signal of the bSSFP contrast between FA's 0-180° with TR=3 ms and TE=1.4 ms, for liver, lesion muscle and fat. Implemented T1 and T2 values are given in the legend. The T1/T2 contrast of the bSSFP sequence illustrates adequate contrast between liver and lesion. Between FA=20° and 80, the largest difference in contrast between liver and lesion is visible. The maximum contrast was found at FA=50°.